A Sparsity Regularization and Total Variation Based Computational Framework for the Inverse Medium Problem in Scattering

Florian Bürgel*, Kamil S. Kazimierski-Hentschel†, Armin Lechleiter‡

August 5, 2016

Abstract

We present a computational framework for the inverse medium problem in scattering, i. e. we look at discretization, reconstruction and numerical performance. The Helmholtz equation in two and three dimensions is used as a physical model of scattering. Point sources as well as plane waves are taken into account as incident fields. Further, near and far field measurements are considered. For the reconstruction of the medium, we set up a variational regularization scheme. The underlying paradigm is, roughly speaking, to minimize the discrepancy between the reconstruction and measured data while, at the same time, taking into account various structural a-priori information via suitable penalty terms. In particular, the involved penalty terms are designed to promote information expected in real-world environments. To this end, a combination of sparsity promoting terms, total variation, and physical bounds of the inhomogeneous medium, e. g. positivity constraints, is employed in the regularization penalty. A primal-dual algorithm is used to solve the minimization problem related to the variational regularization. The computational feasibility, performance and efficiency of the proposed approach is demonstrated for synthetic as well as experimentally measured data (from Institute Fresnel) in two and three dimensions.

Keywords Inverse Scattering Problem, Sparsity Regularization, Total Variation, Primal-Dual Algorithm

1 Introduction

Inverse medium scattering problems seek to identify the refractive index of a penetrable medium from measurements of waves scattered from that medium. In acoustics, such parameter identification problems for instance are crucial for various non-destructive testing procedures based on ultrasound measurements. However, the numerical treatment of inverse medium scattering problems is challenging due to their intrinsic non-linearity and ill-posedness. Further, any inversion algorithm in addition needs to cope with huge system sizes arising after discretization. This is especially true for problems modelling all three space dimensions. In this paper, we propose a complete computational framework for inverse medium scattering at fixed frequency. The employed methods allow to take into account a-priori known structural properties of the searched-for refractive index in the variational reconstruction step via suitable penalty terms. Such properties for instance include (physical) bounds for the values of the refractive index, its sparsity in an a-priori known basis, or the presence of sharp edges.

Numerous algorithms solving inverse medium scattering problems are already established, all having specific advantages and disadvantages. A first class of algorithms (including ours) exploits Fréchet differentiability of the operator mapping the refractive index to the measured data. This allows to set up one of the various existing variants of regularized Newton-like inversion schemes that are typically locally convergent, see [CK13, Hoh01].

*Center for Industrial Mathematics, University of Bremen, Germany, fbuergel@uni-bremen.de.

†Institute of Mathematics and Scientific Computing, University of Graz, Austria, kazimier@uni-graz.at. The Institute of Mathematics and Scientific Computing is a member of NAWI Graz (`www.nawigraz.at`) and BioTechMed Graz (`www.biotechmed.at`).

‡Center for Industrial Mathematics, University of Bremen, Germany, lechleiter@math.uni-bremen.de.

This class includes popular techniques as Kleinman and van den Berg's CG-based modified gradient method or Gutman and Klibanov's simplified gradient method. A second class of algorithms implements constructive uniqueness proofs for (features of) the refractive index, see, e. g. [dLS+16], which also includes so-called quantitative methods that merely identify spatial sets where the refractive index differs from its background values, see [CK13, KG08, KS03]. Finally, a third class of algorithms relies on a high or low frequency assumption to linearize the inversion problem in the corresponding asymptotic regime (e. g., physical optics approximation or Born approximation). This allows to use particular linear inversion methods for inverse medium scattering problems but remains of limited use if the wavelength is in the range of the size of the scattering object.

Whenever an inversion algorithm for the inverse medium scattering problem relies on multi-static data, see Figure 1 below, then it is backed up by uniqueness results for the searched-for refractive index, both in two and three dimensions, see [Häh96, Buk08].

Our minimization-based reconstruction approach is known in inverse problems as (non-linear) Tikhonov regularization. For given near or far field measurements, we rely on the non-linear forward operator mapping the refractive index to the field measurements. As the refractive index n equals one outside the scatterer, we actually prefer to solve for the contrast $q := n^2 - 1$ of compact support, such that the forward operator $\mathcal{F}$ maps q to the measurements. Naturally, we tackle the inversion problem by seeking a contrast q such that $\mathcal{F}(q)$ matches measured data F_{meas}, i. e. $\|\mathcal{F}(q) - F_{\text{meas}}\|$ is small in some appropriate norm. To cope with ill-posedness (i. e., instability) of the inversion problem, this functional must be stabilized by adding a suitable penalty term, see [EHN96]. Considering sparse refractive indices with respect to a pixel or wavelet basis, it is by now well-known that traditionally choosing the square of a Hilbert space norm yields worse results than choosing ℓ^p-norms for $p \in [1, 2)$ close to one, see [LKK13] for a resulting algorithm based on soft-shrinkage iteration. We show in this paper that including further a-priori features of the refractive index further improves the reconstruction quality. This allows for instance to join total variation based with sparsity-promoting regularization. However, coping with additional penalties requires to use a more general minimization algorithm than the soft-shrinkage iteration used in [LKK13]. To this end, we rely on a so-called primal-dual algorithm due to Pock, Bischof, Cremers and Chambolle, see [PCBC09, CP11], which offers enough flexibility for our setting while at the same time improving computation times considerably when compared with soft-shrinkage iterations. This algorithm is hence in particular applicable for three-dimensional inverse scattering problems.

For any inverse problem dealing with parameter identification in differential equations, efficient inversion algorithms rely on an efficient solver for the underlying differential equation. For our setting, we describe solutions to the time-harmonic (direct) scattering problem via the so-called Lippmann-Schwinger equation. This volumetric integral equation can be efficiently discretized using a Fourier-based collocation scheme, which, in its original version, is due to Vainikko [Vai00]. The resulting numerical scheme avoids several disadvantages of standard discretizations as, e. g., finite element or finite difference schemes: Numerical integration of singular functions or of the contrast is avoided, resulting solutions automatically satisfy the radiation condition, and the fast Fourier transform allows for fast matrix-vector multiplication. The resulting dense system matrix hence needs not to be set up, as the arising discrete system can be efficiently tackled by iterative techniques (we rely on the GMRES algorithm).

We will test feasibility and performance of our inversion algorithm via reconstructions from synthetic data in two and three dimensions as well as from experimentally measured data in two dimensions from Institute Fresnel, see [BS01]. Although the run-times should be taken with a pinch of salt because our computations rely on MATLAB, they give an impression of the performance of our algorithm. All numerical examples contained in this paper are computed by the MATLAB toolbox that is available on demand and contains both the mentioned inversion algorithms (primal-dual algorithm, soft-shrinkage iteration), as well as the mentioned integral equation solver for the direct scattering problem.

The rest of this paper is structured as follows: In Section 2 we give a brief introduction to direct and inverse scattering from inhomogeneous media. We tackle the discretization of the forward problem in Section 3 and the reconstruction in Section 4, where we develop a suitable penalty term, show explicitly how to apply the mentioned primal-dual algorithm, and introduce suitable stopping rules. We test our inversion algorithm with synthetic data in Section 5 in two and three dimensions. In Section 6 we apply the inversion algorithm to experimentally measured data.

Notation: We denote standard Lebesgue spaces with integrable pth power on a domain D by $L^p(D)$. The corresponding Sobolev spaces are $W^{s,p}(D)$ for $s \geq 0$ and $p \in [1,\infty]$; for $p = 2$, we abbreviate $H^s(D) = W^{s,2}(D)$. The notation of inner products is $\langle \cdot, \cdot \rangle$. In Section 3 vector and array quantities are denoted by an underlined symbol. To select an element in such quantities we employ an subindex or, where it is beneficial for readability, a bracket, i. e. $\underline{q}_j$ and $\underline{q}(j)$ both denote the jth element of $\underline{q}$. Sometimes we use the notation $f \cdot g$ to point out the pointwise multiplication of functions. The notation $(f\cdot)$ is used to denote the operator of pointwise multiplication (with a function f). In the same vein, $\underline{f} \odot \underline{g}$ and $(\underline{f} \odot\,)$ is used for element-wise multiplication of vector, matrix or array quantities as well as the related operator. Of course, for vectors the notation $(\underline{f} \odot\,)$ is the same as the diagonal operator $\mathrm{diag}(\underline{f})$. Further, except it is explicitly stated otherwise, I denotes the identity operator on an appropriate space.

2 Direct and inverse scattering from inhomogeneous media

This section contains a brief description of the direct and inverse scattering problems we consider in the rest of the paper, following [CK13, Ch. 8]. We consider a time-harmonic incident wave $u^{\mathrm{i}} : \mathbb{R}^d \to \mathbb{C}$ in dimension $d = 2, 3$ with time-dependence $\exp(-\mathrm{i}\omega t)$, where $\omega > 0$ is the angular frequency. Omitting time-dependence, the incident field satisfies the Helmholtz equation with constant wave number $k > 0$,

$$\Delta u^{\mathrm{i}}(x) + k^2 u^{\mathrm{i}}(x) = 0, \quad x \in \mathbb{R}^d. \tag{1}$$

When the incident wave interacts with a scattering object, described by a refractive index function $n : \mathbb{R}^d \to \mathbb{C}$ which equals 1 outside a bounded domain, a scattered wave u^{s} is generated. Consequently, the total wave

$$u^{\mathrm{t}} := u^{\mathrm{i}} + u^{\mathrm{s}} \tag{2}$$

admits the Helmholtz equation

$$\Delta u^{\mathrm{t}} + k^2 n^2 u^{\mathrm{t}} = 0 \quad \text{in } \mathbb{R}^d \tag{3}$$

and the scattered wave u^{s} satisfies Sommerfeld's radiation condition

$$\lim_{|x|\to\infty} |x|^{(d-1)/2} \left(\frac{\partial}{\partial |x|} - \mathrm{i}k \right) u^{\mathrm{s}}(x) = 0, \tag{4}$$

uniformly in all directions $\hat{x} = x/|x| \in \mathbb{S} := \{y \in \mathbb{R}^d : |y| = 1\}$, where $|y| := \sqrt{y_1^2 + \ldots + y_d^2}$. (By abuse of notation, we do not explicitly denote the dimension of the sphere.) The latter condition implies that u^{s} behaves like an outgoing spherical wave with a far field $u^\infty : \mathbb{S} \to \mathbb{C}$,

$$u^{\mathrm{s}}(r\hat{x}) = \frac{\exp(\mathrm{i}kr)}{r} \left(u^\infty(\hat{x}) + \mathcal{O}\left(\frac{1}{r}\right) \right) \quad \text{as } r \to \infty, \text{ uniformly in } \hat{x}.$$

The direct scattering problem is defined as finding a solution u to equations (2)–(4). Instead of considering the above PDE directly, the problem can be reformulated as the equivalent Lippmann-Schwinger equation, which will be introduced in the next section. Therefore, we solve the direct scattering problem by solving the related Lippmann-Schwinger equation. Throughout this paper, we make the quiet assumption that the refractive index n is piece-wise continuous in $\mathbb{R}^d$ such that the contrast

$$q := n^2 - 1 \quad \text{in } \mathbb{R}^d$$

has compact support and satisfies that $1 + \mathrm{Re}(q) = \mathrm{Re}(n^2) > 0$ and $\mathrm{Im}(q) = \mathrm{Im}(n^2) \geq 0$.

Inverse problem and experimental data Clearly, the total field u^{t}, modeled by the solution to (3)–(4) is a quantity, which is accessible to physical measurements. Here, we further assume that the incident field itself can also be made accessible, e. g., by reference measurements without the scattering object. Consequently, due to the equation $u^{\mathrm{s}} = u^{\mathrm{t}} - u^{\mathrm{i}}$ we assume in the sequel that (near or far field) measurements of the scattered field are available. These measurements of the scattered field are then used as data for the following inverse

problem: Reconstruct the contrast function q from several measurements of the scattered field. Since we aim to reconstruct a space-dependent function q, we will generally require multi-static measurements, which means that we assume to know measurements of scattered fields for several incident fields. The experimental set-up is shown in Fig. 1.

The introduced Helmholtz equation models two physical settings: Firstly, the equation describes acoustic waves with fixed frequency that are interacting with an inhomogeneous medium with constant density, both in two and three dimensions. Secondly, it can further be used to describe scattering of electromagnetic waves in transverse magnetic (TM) polarization from some penetrable non-magnetic material independent of one space direction. Note that the second case fits to the experimental data measured in TM polarization by the Institute Fresnel, see [BS01], which we consider in Section 6.

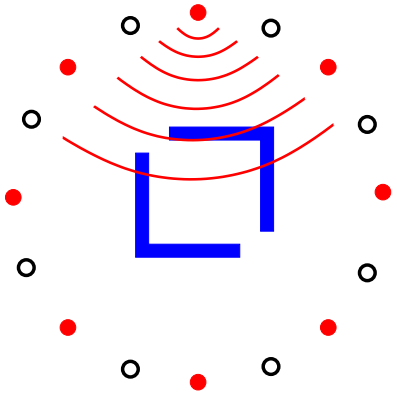

Figure 1: Measurement set-up for multi-static measurements: Several transmitters (red filled circles) propagate incident fields one after the other and the generated scattered fields are measured by several receivers (black hollow circles).

3 Discretization of the forward problem

In this section we tackle the direct scattering problem and discuss its analysis and discretization. We approach the scattering problem by means of the Lippmann-Schwinger equation that equivalently describes the solution to (3). To this end, we consider the volume potential for the radiating fundamental solution of the Helmholtz equation. For the discretization of the related integral equation a collocation scheme similar to the one in [Vai00] is considered. As we will see later, approaching the solution of the direct scattering problem via an integral equation allows for an efficient solution of the inverse medium problem, since the involved wave fields and the contrast are considered within the medium on the same mesh. The final aim of this section is to present continuous and discretized versions of the forward operator of the scattering problem, its Fréchet derivative, and the adjoint of that derivative. The material of this section follows [LKK13, Vai00], and [CK13, Ch. 8].

3.1 Lippmann-Schwinger equation

As we aim to reconstruct the contrast q from indirect measurements, we assume to a-priori possess information about a region of interest (ROI) denoted by $D \subset \mathbb{R}^d$ containing the support of the contrast q. Without loss of generality we further assume that D itself is strictly contained in a ball with radius R centered in the origin

$$B_R := \{x \in \mathbb{R}^d : |x| < R\}.$$

For the sake of simplicity, we set

$$D := \frac{1}{\sqrt{2}}\,[-R, R)^d \tag{5}$$

to be the biggest cube contained in $\overline{B_R}$. By Φ we denote the radiating fundamental solution of the Helmholtz equation,

$$\Phi(x) = \begin{cases} \frac{\mathrm{i}}{4} H_0^{(1)}(k|x|) & \text{if } x \in \mathbb{R}^2,\ x \neq 0, \\ \frac{1}{4\pi} \frac{\exp(\mathrm{i}k|x|)}{|x|} & \text{if } x \in \mathbb{R}^3,\ x \neq 0, \end{cases} \tag{6}$$

where $H_0^{(1)}$ is the Hankel function of first kind and order 0. The fundamental solution defines the volume potential V by

$$v(x) := (Vf)(x) := k^2 \int_D \Phi(x-y) f(y)\,\mathrm{d}y, \quad x \in \mathbb{R}^d. \tag{7}$$

Remark 3.1. *For a function $f \in L^t(D)$ with $t > 1$ the volume potential $v = Vf$ belongs to $W^{2,t}_{\mathrm{loc}}(\mathbb{R}^d) = \{v : \mathbb{R}^d \to \mathbb{C} :\ v|_B \in W^{2,t}(B)$ for all balls $B \subset \mathbb{R}^d\}$ if the function is extended by zero outside of D. Moreover, the function v is the unique radiating solution to $\Delta v + k^2 v = -k^2 f$ in $L^t(\mathbb{R}^d)$, see [LKK13, CK13]. Thus, the*

radiating scattered field u^{s} can be found as a solution of the Lippmann-Schwinger equation: By (3) *and* (1), *there holds $\Delta u^{\mathrm{s}} + k^2 u^{\mathrm{s}} = -k^2 q(u^{\mathrm{i}} + u^{\mathrm{s}})$, such that $u^{\mathrm{s}} - V(q \cdot u^{\mathrm{s}}) = V(q \cdot u^{\mathrm{i}})$ holds in $\mathbb{R}^d$. The corresponding equation for the total field reads $u^{\mathrm{t}} - V(q \cdot u^{\mathrm{t}}) = u^{\mathrm{i}}$ in $\mathbb{R}^d$, see [CK13].*

We consider this integral equation in D. Under the assumption that $\mathrm{Im}(q) \geq 0$ in D it is then well-known that the Lippmann-Schwinger equation is uniquely solvable for all right-hand sides.

Theorem 3.2 (Existence and uniqueness of solution [LKK13])**.** *Let the contrast q be in $L^p(D)$ for $p > d/2 (\geq 1)$ such that $\mathrm{Im}(q) \geq 0$ in D and extend q by zero to all of $\mathbb{R}^d$. Furthermore choose $t > \max\{p/(p-1), 2d/(d+2)\}$ and an incident field $u^{\mathrm{i}} \in L^t(D)$. Then the Lippmann-Schwinger equation*

$$v - V(q \cdot v) = V(q \cdot u^{\mathrm{i}}) \quad \text{in } L^t(D) \tag{8}$$

has a unique solution $v \in L^t(D)$. Setting $u^{\mathrm{s}} := V(q \cdot (v + u^{\mathrm{i}}))$ defines a radiating solution $u^{\mathrm{s}} \in W^{2,tp/(t+p)}_{\mathrm{loc}}(\mathbb{R}^d)$ to the Helmholtz equation $\Delta u^{\mathrm{s}} + k^2(1+q)u^{\mathrm{s}} = -k^2 q u^{\mathrm{i}}$ in $L^t_{\mathrm{loc}}(\mathbb{R}^d)$.

3.2 Periodization of the volume potential

Remember that $\mathrm{supp}(q) \subset D$. This implies that $\mathrm{supp}(f) \subset D$ for $f = qu^{\mathrm{i}}$ or $f = qu^{\mathrm{s}}$. Plugging such f into the integral operator V from (7), we conclude that the source term f vanishes outside $B_R \supset D$. In addition, a close inspection of (7) reveals that to evaluate $Vf(x)$ the values of Φ do only have to be known in the ball B_{2R}. This is the case since if the points x, y are in B_R the difference $x - y$ belongs to B_{2R}. Consequently, as in [Vai00], we define a modified kernel Φ_{2R} by cutting off Φ outside of B_{2R} and multiplying it by k^2,

$$\Phi_{2R}(x) := \begin{cases} k^2 \Phi(x) & \text{if } x \in B_{2R}, \\ 0 & \text{if } x \in \overline{D_{2R}} \setminus B_{2R}, \end{cases} \tag{9}$$

This allows us to define an equivalent periodized integral operator V_{2R} in the computational domain D_{2R}, where D_{2R} is a square or cube with side length $4R$ containing B_{2R},

$$D_{2R} := \{x \in \mathbb{R}^d : -2R \leq x_\ell < 2R,\ \ell = 1, \ldots, d\}.$$

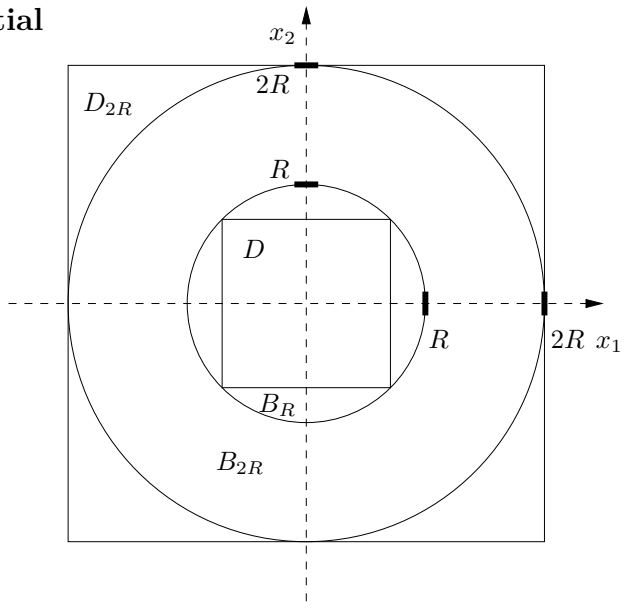

Figure 2: Areas in 2D: computational domain D_{2R}, region of interest D and balls B_R and B_{2R}.

The relations between the computational domain D_{2R}, the region of interest D and the balls B_R and B_{2R}, are illustrated in Fig. 2. Extending both Φ_{2R} and q from D_{2R} to $\mathbb{R}^d$ as $4R$-periodic functions with respect to $x_1, \ldots, x_d$, we define this periodized integral operator $V_{2R} : L^2(D_{2R}) \to L^2(D_{2R})$ by

$$(V_{2R} f)(x) := \int_{D_{2R}} \Phi_{2R}(x - y) f(y)\, \mathrm{d}y, \quad x \in D_{2R}. \tag{10}$$

We use the same symbol for the original and extended versions since it is clear form the context which one is meant.

As discussed in the beginning of this section, $(Vf)|_D = (V_{2R} f)|_D$ for all $f \in L^2(D)$ (and even for all $f \in B_R$), if they are extended by zero to all of D_{2R}. Since, the operator V_{2R} is a $4R$-periodic convolution operator acting on functions in $L^2(D_{2R})$ it can be evaluated by means of the convolution theorem. To that end, we consider the complete orthogonal system in $L^2(D_{2R})$:

$$\varphi_j(x) := \frac{1}{(4R)^{d/2}} \exp\left(\frac{2\pi \mathrm{i}}{4R} \langle j, x \rangle\right), \quad j \in \mathbb{Z}^d. \tag{11}$$

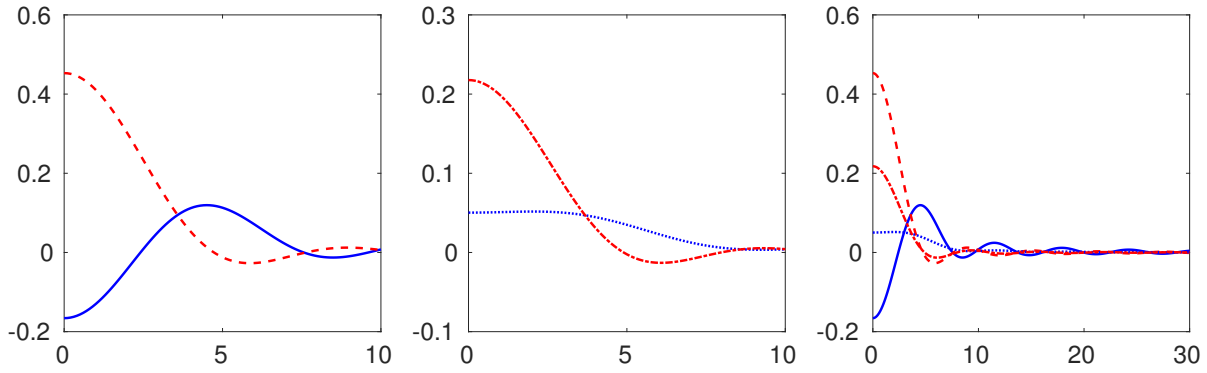

(a) 2D. (b) 3D. (c) Decay in 2D and 3D.

Figure 3: Real (blue solid and dotted) and imaginary part (red dashed and dash-dotted) of Fourier coefficients $\hat{\Phi}_{2R}$ over $p_j = \pi|j| \geq 0$ with $R = 1$, $k = 1$, such that $\kappa = 2Rk = 2$. We see that the Fourier coefficients decay in j.

Then for every $f \in L^2(D_{2R})$ the representation $f = \sum_{j\in\mathbb{Z}^d} \hat{f}(j)\varphi_j$ holds, where the Fourier coefficients $\hat{f}(j)$ are defined as $\int_{D_{2R}} f\,\overline{\varphi_j}\,\mathrm{d}x$. Further, the convolution theorem for that system shows that the Fourier coefficients of $V_{2R}f$ are given via

$$\widehat{V_{2R}f}(j) = (4R)^{d/2}\,\hat{\Phi}_{2R}(j)\,\hat{f}(j), \quad j \in \mathbb{Z}^d. \tag{12}$$

Further, the Fourier coefficients of the convolution kernel can be explicitly computed, see [Vai00, Hoh01]. They decay in j as $|\hat{\Phi}_{2R}(j)| \leq C(1+|j|)^{-3/2}$ for $d = 2$ and $|\hat{\Phi}_{2R}(j)| \leq C(1+|j|)^{-2}$ for $d = 3$, see Fig. 3. To omit repeating the factor $(4R)^{d/2}$ we define

$$\Psi_{2R} := (4R)^{d/2}\,\hat{\Phi}_{2R} \tag{13}$$

and $p_j := \pi|j|$ and $\kappa := 2Rk$. Then in the two-dimensional setting

$$\Psi_{2R}(j) = \begin{cases} \frac{\kappa^2}{p_j^2-\kappa^2}\left(1 + \frac{\mathrm{i}\pi}{2}\left[p_j J_1(p_j)H_0^{(1)}(\kappa) - \kappa J_0(p_j)H_1^{(1)}(\kappa)\right]\right) & \text{if } p_j \neq \kappa, \\ \frac{\mathrm{i}\pi\kappa^2}{4}\left[J_1(\kappa)H_1^{(1)}(\kappa) + J_0(\kappa)H_0^{(1)}(\kappa)\right] & \text{if } p_j = \kappa, \end{cases} \quad \text{for } d = 2, \tag{14}$$

where J_ν and $H_\nu^{(1)}$ are the cylindrical Bessel and Hankel functions. Further, in three dimensions $\Psi_{2R}(0) = (1-\mathrm{i}\kappa)\exp(\mathrm{i}\kappa) - 1$ and

$$\Psi_{2R}(j) = \begin{cases} \frac{\kappa^2}{p_j^2-\kappa^2}\left(1 - \mathrm{e}^{\mathrm{i}\kappa}\left[\cos(p_j) - \frac{\mathrm{i}\kappa}{p_j}\sin(p_j)\right]\right) & \text{if } 0 \neq p_j \neq \kappa, \\ \frac{1}{2}\mathrm{e}^{\mathrm{i}\kappa}\left(\kappa\sin(\kappa) + \mathrm{i}[\kappa\cos(\kappa) - \sin(\kappa)]\right) & \text{if } p_j = \kappa, \end{cases} \quad \text{for } d = 3. \tag{15}$$

Note the correction in the above formula for $d = 3$ in case of $p_j = \kappa$ of the value given in [Vai00, Hoh01].

3.3 Discretization of the Lippmann-Schwinger equation

We exploit the convolution structure of the volume potential for its discretization via the fast Fourier transform. The periodized volume potential V_{2R} allows to consider in D_{2R} the Lippmann-Schwinger equation corresponding to (8),

$$v - V_{2R}(q\cdot v) = V_{2R}(q\cdot u^{\mathrm{i}}) \quad \text{in } L^2(D_{2R}). \tag{16}$$

As previously, the functions q and qu^{i} are understood to be extended $4R$-periodically to $\mathbb{R}^d$ where necessary. As in [Vai00], one shows that (16) is well-posed in $L^t(D_{2R})$ whenever (8) is well-posed in $L^t(D)$. Moreover, a solution v to (16) equals the scattered field u^{s} solving (8) on B_R, and in particular on D.

To discretize (8), we define in the domain D_{2R} a mesh of N^d regularly spaced collocation points with step size $h_N := 4R/N$ for $N \in \mathbb{N}$,

$$x_j^{(N)} := h_N j = \frac{4R}{N} j \subset D_{2R} \quad \text{for } j \in \mathbb{Z}_N^d := \left\{ j = (j_1, \dots, j_d)^\top \in \mathbb{Z}^d : -\frac{N}{2} \le j_\ell < \frac{N}{2}, \ell = 1, \dots, d \right\}. \quad (17)$$

Moreover, we introduce the approximation space

$$T_N := \left\{ \sum_{j \in \mathbb{Z}_N^d} c_j \varphi_j : c_j \in \mathbb{C} \right\}, \quad N \in \mathbb{N}, \quad (18)$$

which is, roughly speaking, the space of trigonometric polynomials up to degree $N/2$. Clearly, since the basis functions φ_j from (11) are orthonormal, every $v_N \in T_N$ has a representation $v_N = \sum_{j \in \mathbb{Z}_N^d} c_j \varphi_j$, where the representation coefficients c_j are unique and are just the Fourier coefficients $\hat{v}_N(j) = \int_{D_{2R}} v_N \overline{\varphi_j} \, \mathrm{d}x$ of v_N. The key to the discretization of the Lippmann-Schwinger equation is the fact that every function in T_N can equivalently be characterized by its Fourier coefficients as well as its point values on the above introduced mesh. To be exact, for every set of point values $\underline{v}_N := (\underline{v}_N(j))_{j \in \mathbb{Z}_N^d}$ there exists exactly one $v_N \in T_N$ such that $v_N(x_j^{(N)}) = \underline{v}_N(j)$. Since $\varphi_j(x_\ell^{(N)}) = 1/(4R)^{d/2} \omega_N^{-j \cdot \ell}$ with $\omega_N = \exp(-2\pi \mathrm{i}/N)$ and $j, \ell \in \mathbb{Z}^d$, the following relations hold between the collocation values and the Fourier coefficients of v_N:

$$v_N(x_\ell^{(N)}) = \sum_{j \in \mathbb{Z}_N^d} \hat{v}_N(j) \varphi_j(x_l^{(N)}) = \frac{1}{(4R)^{d/2}} \sum_{j \in \mathbb{Z}_N^d} \hat{v}_N(j) \, \omega_N^{-j \cdot \ell}, \quad \hat{v}_N(j) = \frac{(4R)^{d/2}}{N^d} \sum_{\ell \in \mathbb{Z}_N^d} v_N(x_\ell^{(N)}) \, \omega_N^{j \cdot \ell}. \quad (19)$$

Clearly, one recognizes in these equations, up to a scaling factor, the discrete forward and inverse Fourier transform.

To discretize (16) we replace v there by an $v_N \in T_N$. Still, the term qv_N will in general fail to belong to T_N and we will not be able to use fast evaluation of the operator V_{2R}. To remedy this we project qv_N onto T_N. With similar argumentation we project qu^{i} too. However, it is of uttermost importance that not the standard projection is used but the interpolation projection Q_N, which for piece-wise continuous f is defined by

$$(Q_N f)(x_j^{(N)}) := f(x_j^{(N)}), \quad j \in \mathbb{Z}_N^d.$$

This interpolation then discretizes the periodized integral equation (16) by collocation,

$$v_N - V_{2R}(Q_N(q \cdot v_N)) = V_{2R}(Q_N(q \cdot u^{\mathrm{i}})) \text{ in } T_N. \quad (20)$$

The point evaluations of v, u^{i}, and q at the grid points $x_j^{(N)}$ are denoted $\underline{v}_N$, $\underline{u}_N^{\mathrm{i}}$, and $\underline{q}_N$ and are d-dimensional complex-valued arrays of size $N \times N$ in 2D and $N \times N \times N$ in 3D. We write $\mathbb{C}_N^d$ for the space of such arrays. Of course when considered as elements of a vector space these arrays will still be called vectors. Defining the array Ψ_N via

$$\Psi_N := (\Psi_{2R}(j))_{j \in \mathbb{Z}_N^d},$$

allows the equation (20) to be equivalently reformulated in a fully discrete way,

$$\underline{v}_N - V_N(\underline{q}_N \odot \underline{v}_N) = V_N(\underline{q}_N \odot \underline{u}_N^{\mathrm{i}}) \quad \text{in } \mathbb{C}_N^d, \text{ where } V_N := F_N^{-1}(\Psi_N \odot) F_N. \quad (21)$$

Here, $A \odot B$ denotes the element-wise multiplication of two arrays and $(A \odot)$ the operator of pointwise multiplication with A. Further, F_N denotes the d-dimensional discrete Fourier transform $(F_N x)_l = \sum_{j \in \mathbb{Z}_N^d} x_j \omega_N^{\ell \cdot j}$, where $l \in \mathbb{Z}_N^d$ and $\omega_N = \exp(-2\pi \mathrm{i}/N)$. The changes necessary to evaluate V_N by the fast Fourier transform will be discussed in the next subsection. With respect to the solution method of (21) we remark that the resulting system matrix is a full matrix of size $N^d \times N^d$. Therefore, it is advisable to tackle the arising linear system by an iterative solver. For example, in our numerical experiments we employ the GMRES algorithm.

Convergence analysis of the latter scheme is typically done in the Sobolev spaces $H^s(D_{2R})$, see [Vai00, Hoh01, LN11] for closely related methods. Roughly speaking, the smoother the contrast the higher the

convergence rate: If, e. g., qu^{i} belongs to $H^s(D_{2R})$ with $s > d/2$, then the solution v to (16) belongs to $H^{s+(d+1)/2}(D_{2R})$, $d = 2, 3$, and there is $N_0 \in \mathbb{N}$ such that for all $N \geq N_0$ the solution v_N to (20) exists and satisfies $\|v_N - v\|_{L^2(D_{2R})} \leq CN^{-s-(d+1)/2}\|qu^{\mathrm{i}}\|_{H^s(D_{2R})}$. Of course, the approximation rate is dimension-dependent, similar to the decay rate of the Fourier coefficients of Φ_{2R}, see (14) and (15) in combination with (13).

3.4 Implementation of the collocation scheme

When implementing the discrete scheme (21), two technical issues become quickly evident. Firstly, considering the indexing of the Fourier transforms observes that the standard implementation of the fast Fourier transform (FFT) uses shifted indices as compared to the formulas in (19). Explicitly, FFT uses indices $j_\ell = 0, \ldots, \lceil N/2 \rceil - 1, \lceil -N/2 \rceil, \ldots, -1$, see [FJ05], where discrete Fourier transform employs $j_\ell = \lceil -N/2 \rceil, \ldots, \lceil N/2 \rceil - 1$ as defined in (17). Both issues have to be addressed in efficient implementations. Secondly, at first glance the equation (21) seems to imply that $\underline{v}_N$ has to be solved for the N^d degrees of freedom in $\mathbb{C}^d_N$ related to the point evaluations in the computational domain D_{2R}. However, recalling that by assumption the support of q is contained in D together with (20) reveals that v_N has at most support in D. Therefore, it suffices to consider and store the point evaluations of v_N on D only and extend/restrict them between that space and $\mathbb{C}^d_N$ where necessary for means of (21).

First, we tackle the indexation issue for the discrete Fourier transform. For a d-dimensional array $f \in \mathbb{C}^d_N$ the d-dimensional forward and inverse FFT is defined via $(\mathrm{FFT}_N f)(j) := \sum f(\ell)\, \omega_N^{\ell \cdot j}$ and $(\mathrm{FFT}_N^{-1} f)(j) := \frac{1}{N^d} \sum f(\ell)\, \omega_N^{-j \cdot \ell}$, where $\omega_N = \exp(-2\pi \mathrm{i}/N)$, the summation is carried over all ℓ with $0 \leq \ell_1, \ldots, \ell_d \leq N - 1$ and the evaluation index j is such that $0 \leq j_1, \ldots, j_d \leq N - 1$. Hence, if S_N is the operator on $\mathbb{C}^d_N$ shifting cyclically by $\lceil (N-1)/2 \rceil$ in every dimension, then $F_N = S_N\, \mathrm{FFT}_N\, S_N^{-1}$. This implies that the operator V_N can be implemented via $V_N \underline{f}_N = \mathrm{FFT}_N^{-1} \left[S_N^{-1}(\Psi_N) \odot \mathrm{FFT}_N \underline{f}_N \right]$, since $S_N(A \odot B) = S_N(A) \odot S_N(B)$ and there exist A_1 and A_2, such that A_2 is the entry-wise inverse of A_1, and $S_N \mathrm{FFT}_N = \mathrm{FFT}_N(A_1 \odot\,)$, $\mathrm{FFT}_N S_N^{-1} = (A_2 \odot\,)\mathrm{FFT}_N$. The last statement is true since a circular shift is a circular convolution and a version of the convolution theorem applies to FFT_N.

Concerning the second problem, we introduce restriction operators $\mathcal{R}_N$ that restrict point values $\underline{v}_N \in \mathbb{C}^d_N$ of $v_N \in T_N$ to grid points inside D. The corresponding extension operators $\mathcal{E}_N$ extend point values on grid points inside D by zero to elements of $\mathbb{C}^d_N$. We denote by

$$\mathbb{C}^{N_{\mathrm{D}}} \quad \text{with} \quad N_D := \lfloor N/(2\sqrt{2}) \rfloor^d \tag{22}$$

the space of point values related to grid points $x_j^{(N)}$ inside D. Then $\mathcal{R}_N$ maps $\mathbb{C}^d_N$ into $\mathbb{C}^{N_{\mathrm{D}}}$ and $\mathcal{E}_N$ maps $\mathbb{C}^{N_{\mathrm{D}}}$ into $\mathbb{C}^d_N$. Fig. 4 visualizes the action of $\mathcal{R}_N$ and $\mathcal{E}_N$. Both operators are adjoint to each other with respect to the standard inner products of $\mathbb{C}^d_N$ and $\mathbb{C}^{N_{\mathrm{D}}}$.

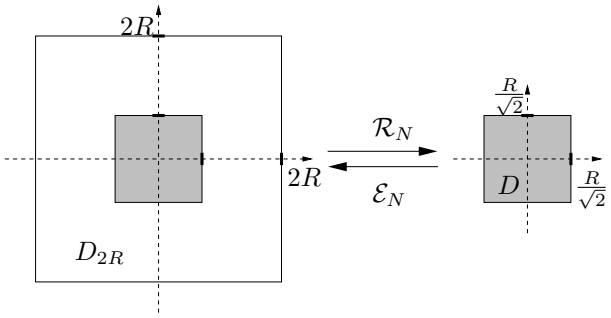

Figure 4: Restriction $\mathcal{R}_N$ (mapping grid values in $\mathbb{C}^d_N$ into $\mathbb{C}^{N_{\mathrm{D}}}$) and extension $\mathcal{E}_N$ (mapping $\mathbb{C}^{N_{\mathrm{D}}}$ into $\mathbb{C}^d_N$) in case $d = 2$.

Altogether, we arrive at the final formulation of the discretized Lippmann-Schwinger equation (21): with

$$\widehat{\Phi}_N := S_N^{-1}(\Psi_N)$$

and

$$V_{N_{\mathrm{D}}} : \mathbb{C}^{N_{\mathrm{D}}} \to \mathbb{C}^{N_{\mathrm{D}}} \quad \text{with} \quad V_{N_{\mathrm{D}}} := \mathcal{R}_N \mathrm{FFT}_N^{-1}(\widehat{\Phi}_N \odot\,)\mathrm{FFT}_N \mathcal{E}_N, \tag{23}$$

it is given by

$$\underline{v}_{N_{\mathrm{D}}} - V_{N_{\mathrm{D}}} \left(\underline{q}_{N_{\mathrm{D}}} \odot \underline{v}_{N_{\mathrm{D}}} \right) = V_{N_{\mathrm{D}}} \left(\underline{q}_{N_{\mathrm{D}}} \odot \underline{u}^{\mathrm{i}}_{N_{\mathrm{D}}} \right) \quad \text{in } \mathbb{C}^{N_{\mathrm{D}}}. \tag{24}$$

3.5 Single-layer and measurement operators for multi-static data

In the last section we presented an efficient way to discretize the physical model for the effects of scattering within the region of interest D. To present the full model, in this section, we discuss the operators involved with the propagation from point sources ("transmitters") to D and the propagation from D to measurement points ("receivers"). Our discussion is focused on the multi-static case, i. e. data originating from several incident fields. In this approach we are motivated by the well-known fact that unique determination of the contrast q without a-priori information requires multi-static scattering data, see, e. g., [CK13, LKK13].

As mentioned in the introduction, the first type of incident fields are point sources $u^{\mathrm{i}}_j(x) = \Phi(x - p_j)$, where Φ is the fundamental solution presented in (6) and $x \in \mathbb{R}^d$, $j = 1, \dots, N_{\mathrm{i}}$. We assume that these N_{i} fields originate from source points p_j outside of $\overline{B_R}$ and are placed on a manifold Γ_{i}. Therefore, linear combinations of the N_{i} fields yield approximations to single-layer potentials on Γ_{i}

$$\mathrm{SL}_{\Gamma_{\mathrm{i}}\to D} : L^2(\Gamma_{\mathrm{i}}) \to L^2(D), \quad (\mathrm{SL}_{\Gamma_{\mathrm{i}}\to D}\, g)(x) := \int_{\Gamma_{\mathrm{i}}} \Phi(x-y) g(y)\, \mathrm{d}S, \quad x \in D. \tag{25}$$

The second type of incident fields are plane waves $u^{\mathrm{i}}_j(x) = \exp(\mathrm{i}k\langle x, \theta_j\rangle)$, radiating from N_{i} directions $\theta_j \in \mathbb{S}$, $j = 1, \dots, N_{\mathrm{i}}$. For plane waves, it is sensible to replace Γ_{i} in (25) by $\mathbb{S}$ and $\Phi(x-y)$ by the plane wave $\exp(\mathrm{i}k\langle x, y\rangle)$. To keep the notation simple, we do not introduce a separate symbol for the single-layer potential, since it is clear from the context which kind of incident fields is used, i. e. for plane waves the symbol $\mathrm{SL}_{\mathbb{S}\to D}$ is employed. In both cases the operator is discretized directly by quadrature resulting in

$$\mathrm{SL}_{N_{\mathrm{i}},N_{\mathrm{D}}} : \mathbb{C}^{N_{\mathrm{i}}} \to \mathbb{C}^{N_{\mathrm{D}}}, \quad (\mathrm{SL}_{N_{\mathrm{i}},N_{\mathrm{D}}}\, \underline{g}_{N_{\mathrm{i}}})(\ell) := \sum_{j=1}^{N_{\mathrm{i}}} \omega^{\mathrm{i}}_j u^{\mathrm{i}}_j(x_\ell) \underline{g}_{N_{\mathrm{i}}}(j)\,, \tag{26}$$

where the weights ω^{i}_j approximate the surface element on Γ_{i} in a neighborhood of p_j. In general, one is well advised to store the operator as matrix. Then the evaluation of the operator reduces to a matrix-vector multiplication.

Having discussed the propagation from the sources to the region of interest, next we consider the operators responsible for the physical action in the region of interest itself. To this end, we remark that for a given incident field the periodized Lippmann-Schwinger equation (16) is uniquely solvable for contrasts q in the closed and convex set

$$L^p_{\mathrm{Im}\geq 0}(D) := \{q \in L^p(D) : \mathrm{Im}(q) \geq 0 \text{ in } D\} \subset L^p(D), \quad p > d/2,$$

where, as previously, such contrasts are extended by zero to the computational domain D_{2R}. The restriction to D of such solution coincides with the corresponding scattered field on D. Let $(q\,\cdot)$ denote the operator of pointwise multiplication with the contrast q, then the operator

$$T_q : L^t(D) \to W^{2,tp/(t+p)}(D), \quad T_q := (I - V_{2R}(q\,\cdot))^{-1}$$

denoting the inverse of the left hand side of (16) is bounded for t large enough, cf. Theorem 3.2. Applying T_q to an incident field yields the corresponding total field on D, i. e., $u^{\mathrm{t}}|_D = T_q\big(\mathrm{SL}_{\Gamma_{\mathrm{i}}\to D}\, g\big)$, cf. Remark 3.1. The discretization of T_q is given by

$$T_{\underline{q}} : \mathbb{C}^{N_{\mathrm{D}}} \to \mathbb{C}^{N_{\mathrm{D}}}, \quad T_{\underline{q}} := (I - V_{N_{\mathrm{D}}}(\underline{q} \odot\,))^{-1}, \quad \text{where } \underline{q} \in \mathbb{C}^{N_{\mathrm{D}}}. \tag{27}$$

With the Lippmann-Schwinger equation (24) for the scattering field and Remark 3.1 in mind it is clear that the mappings $T_{\underline{q}}\,\mathrm{SL}_{N_{\mathrm{i}},N_{\mathrm{D}}}$ and $(I + T_{\underline{q}} V_{N_{\mathrm{D}}}(\underline{q} \odot\,))\,\mathrm{SL}_{N_{\mathrm{i}},N_{\mathrm{D}}}$ coincide. The former is more convenient for analytical purposes, the latter is more suitable for numerics.

Finally, we model the near and far field measurement operators. The near field measurements of the scattered field u^{s} are assumed to be carried out on a non-empty, closed Lipschitz surface Γ_{s}. Assuming that Γ_{s} does not intersect $\overline{D}$, we choose N_{s} points ("receivers") $x_1, \dots, x_{N_{\mathrm{s}}}$ on Γ_{s}. Then, near field measurements are modeled via the representation (8) of the scattered field, which implies that

$$V_{D\to\Gamma_{\mathrm{s}}} : L^2(D) \to L^2(\Gamma_{\mathrm{s}}), \quad (V_{D\to\Gamma_{\mathrm{s}}} f)(x) := k^2 \int_D \Phi(x-y) f(y)\, \mathrm{d}x, \quad x \in \Gamma_{\mathrm{s}}, \tag{28}$$

satisfies $u^{\mathrm{s}}|_{\Gamma_{\mathrm{s}}} = V_{D\to\Gamma_{\mathrm{s}}}(q\cdot u^{\mathrm{t}}) = V_{D\to\Gamma_{\mathrm{s}}}(q\cdot T_q(\mathrm{SL}_{\Gamma_{\mathrm{i}}\to D}\, g))$. To model far field measurements, we replace Γ_{s} by $\mathbb{S}$, choose N_{s} directions $\hat{x}_1,\dots,\hat{x}_{N_{\mathrm{s}}}\in\mathbb{S}$, and replace $\Phi(x-y)$ in the definition of $V_{D\to\Gamma_{\mathrm{s}}}$ by $\gamma\cdot\exp(-\mathrm{i}k\langle\hat{x}_\ell, x_j^{(N)}\rangle)$, where the dimension-dependent factor γ is $\exp(\mathrm{i}\pi/4)/\sqrt{8\pi k}$ in 2D and $1/(4\pi)$ in 3D, see [CK13, Ch. 3.5, 8.4]. In a similar way as for the single-layer potential, we do not introduce an explicit symbol for far field measurements. Explicitly we employ $V_{D\to\mathbb{S}}$ to that end. As for the single-layer potential we also discretize the measurement operator by quadrature,

$$V_{N_{\mathrm{D}},N_{\mathrm{s}}}:\mathbb{C}^{N_{\mathrm{D}}}\to\mathbb{C}^{N_{\mathrm{s}}},\quad (V_{N_{\mathrm{D}},N_{\mathrm{s}}}\underline{f}_{N_{\mathrm{D}}})(\ell) := h_N^d k^2 \sum\nolimits_{j\in\mathbb{Z}_N^d} \Phi(x_\ell - x_j^{(N)})\underline{f}_{N_{\mathrm{D}}}(j), \tag{29}$$

where h_N^d is the dth power of the grid size introduced in (17) and $x_j^{(N)}$ are the points introduced in that same equation. For near/far field measurements Φ has to be chosen/modified according to the remarks of the last paragraph. As the discretization of the single-layer potential the measurement operator $V_{N_{\mathrm{D}},N_{\mathrm{s}}}$ is also in general stored as a matrix. Consequently, its evaluation is a matrix-vector multiplication.

The scattered field u^{s} on Γ_{s} (or the far field on $\mathbb{S}$) in a multi-static setting then equals $u^{\mathrm{s}}|_{\Gamma_{\mathrm{s}}} = V_{D\to\Gamma_{\mathrm{s}}}(q\cdot u^{\mathrm{t}}) = V_{D\to\Gamma_{\mathrm{s}}}\big(q\cdot T_q\big(\mathrm{SL}_{\Gamma_{\mathrm{i}}\to D}\, g\big)\big)$, and is therefore approximated by its discrete variant $V_{N_{\mathrm{D}},N_{\mathrm{s}}}\big(\underline{q}\odot T_{\underline{q}}\big(\mathrm{SL}_{N_{\mathrm{i}},N_{\mathrm{D}}}\,\underline{g}_{N_{\mathrm{i}}}\big)\big)$.

3.6 The forward scattering operator and its derivative

With the operators discussed in the last subsection and their discretizations we are now ready to present the full, nonlinear, multi-static contrast-to-measurement operator

$$\mathcal{F}: L^p_{\mathrm{Im}\geq 0}(D)\to \mathrm{HS}(L^2(\Gamma_{\mathrm{i}}),L^2(\Gamma_{\mathrm{s}})),\quad \mathcal{F}(q) := V_{D\to\Gamma_{\mathrm{s}}}(q\cdot)T_q\,\mathrm{SL}_{\Gamma_{\mathrm{i}}\to D},$$

where HS is the space of Hilbert-Schmidt operators from $L^2(\Gamma_{\mathrm{i}})$ into $L^2(\Gamma_{\mathrm{s}})$. Consequently, for every q the value $\mathcal{F}(q)$ is a bounded, linear operator from $L^2(\Gamma_{\mathrm{i}})$ to $L^2(\Gamma_{\mathrm{s}})$. The corresponding discretized operator

$$\underline{\mathcal{F}}:\mathbb{C}^{N_{\mathrm{D}}}\to\mathbb{C}^{N_{\mathrm{D}}\times N_{\mathrm{i}}},\quad \underline{\mathcal{F}}(\underline{q}) := V_{N_{\mathrm{D}},N_{\mathrm{s}}}(\underline{q}\odot)T_{\underline{q}}\,\mathrm{SL}_{N_{\mathrm{i}},N_{\mathrm{D}}} \tag{30}$$

maps $\underline{q}\in\mathbb{C}^{N_{\mathrm{D}}}$, the point evaluations of the contrast on D, to the measurement data, a matrix in $\mathbb{C}^{N_{\mathrm{s}}\times N_{\mathrm{i}}}$.

After presenting the forward operator, we now direct our attention to its derivative and its adjoint. For $q\in L^p_{\mathrm{Im}\geq 0}(D)$ with $p>d/2$ the operator $\mathcal{F}$ is Fréchet differentiable [LKK13] with

$$\mathcal{F}'(q)[h]g = V_{D\to\Gamma_{\mathrm{s}}}(I+(q\cdot)T_qV_{2R})(h\cdot)T_q\,\mathrm{SL}_{\Gamma_{\mathrm{i}}\to D}\,g,\quad g\in L^2(\Gamma_{\mathrm{i}}) \tag{31}$$

and the linear operator $\mathcal{F}'(q)$ from $L^p(D)$ into $\mathrm{HS}(L^2(\Gamma_{\mathrm{i}}),L^2(\Gamma_{\mathrm{s}}))$ is bounded. To formally deduct the last formula the product rule $[F\odot G]'(q)[h] = F(q)\odot G'(q)[h] + F'(q)[h]\odot G(q)$ and the inverse rule $(F^{-1})'(q)[h] = F(q)^{-1}\,F'(q)[h]\,F(q)^{-1}$ are helpful. Further, the derivative of the discretized operator $\underline{\mathcal{F}}$ is given via

$$\underline{\mathcal{F}}'(\underline{q})[\underline{h}] = A_{N_{\mathrm{D}},N_{\mathrm{s}}}(\underline{h}\odot)B_{N_{\mathrm{D}},N_{\mathrm{i}}}\quad \text{in } \mathbb{C}^{N_{\mathrm{s}}\times N_{\mathrm{i}}} \text{ for } \underline{h}\in\mathbb{C}^{N_{\mathrm{D}}} \tag{32}$$

where

$$A_{N_{\mathrm{D}},N_{\mathrm{s}}} := V_{N_{\mathrm{D}},N_{\mathrm{s}}}\big(I+(\underline{q}\odot)T_{\underline{q}}V_{N_{\mathrm{D}}}\big)\in\mathbb{C}^{N_{\mathrm{i}}\times N_{\mathrm{D}}}\quad\text{and}\quad B_{N_{\mathrm{D}},N_{\mathrm{i}}} := T_{\underline{q}}\,\mathrm{SL}_{N_{\mathrm{i}},N_{\mathrm{D}}}\in\mathbb{C}^{N_{\mathrm{D}}\times N_{\mathrm{i}}}.$$

The reader should be aware that $A_{N_{\mathrm{D}},N_{\mathrm{s}}}$ and $B_{N_{\mathrm{D}},N_{\mathrm{i}}}$ are functions of the discretized contrast $\underline{q}$. Due to the above factorization the adjoint $[\underline{\mathcal{F}}'(\underline{q})]^*$ of the derivative with respect to the standard inner products is given by

$$[\underline{\mathcal{F}}'(\underline{q})]^*\underline{H} = \sum_{j=1}^{N_{\mathrm{s}}}\sum_{\ell=1}^{N_{\mathrm{i}}}\underline{H}_{j,\ell}\,\overline{A_{N_{\mathrm{D}},N_{\mathrm{s}}}(j,\cdot)}\,\overline{B_{N_{\mathrm{D}},N_{\mathrm{i}}}(\cdot,\ell)}\quad\text{for } \underline{H}\in\mathbb{C}^{N_{\mathrm{s}}\times N_{\mathrm{i}}},$$

where $A(j,\cdot)$ denotes the jth row and $A(\cdot,\ell)$ the ℓth column of a matrix A. To see this, we recall that $A(h\odot)B = \sum_i h_i A(\cdot,i)B(i,\cdot)$ holds.

Up until this point all complex spaces involved in definitions of discretized operators were equipped with the standard inner product. However, for the definition of the full forward operator $\underline{\mathcal{F}}$ one could also consider

weighted versions which mimic the behavior of the spaces involved in the definition of the operator $\mathcal{F}$. The discretization of the norm in the pre-image space $L^p_{\mathrm{Im}\geq 0}$ yields the norm

$$\|x\|_{\mathrm{roi},p} := \left(h_N^d \sum_i |x_i|^p \right)^{\frac{1}{p}}, \quad x \in \mathbb{C}^{N_\mathrm{D}},$$

for the space $\mathbb{C}^{N_\mathrm{D}}$. In particular for $p = 2$ the following inner product discretization

$$\langle x, y \rangle_{\mathrm{roi}} := h_N^d \sum_i x_i \overline{y_i}, \quad x, y \in \mathbb{C}^{N_\mathrm{D}}, \tag{33}$$

is sensible. For the space $\mathbb{C}^{N_\mathrm{s} \times N_\mathrm{i}}$ we propose the discretization of the inner product in $\mathrm{HS}(L^2(\Gamma_\mathrm{i}), L^2(\Gamma_\mathrm{s}))$ by the weighted Frobenius product

$$\langle A, B \rangle_{\mathrm{dis}} := \mathrm{trace}\big(B^* \, \omega^\mathrm{s} \, A\big) = \sum_{j=1}^{N_\mathrm{s}} \omega_j^\mathrm{s} \sum_{\ell=1}^{N_\mathrm{i}} A_{j\ell} \overline{B_{j\ell}}, \quad A, B \in \mathbb{C}^{N_\mathrm{s} \times N_\mathrm{i}}, \tag{34}$$

where the diagonal weight matrix $\omega^\mathrm{s} = \mathrm{diag}((\omega_j^\mathrm{s})_{j=1}^{N_\mathrm{s}})$ is due to the weights approximating the surface element on Γ_s. The letter combination "dis" is due to the fact that the induced norm $\|\cdot\|_{\mathrm{dis}}$ is used as discrepancy term in the reconstruction scheme discussed in the next section. Formally, the change of norms can be incorporated into the above definitions by introducing the embeddings $\iota_1 : (\mathbb{C}^{N_\mathrm{D}}, \|\cdot\|_{\mathrm{roi},p}) \to (\mathbb{C}^{N_\mathrm{D}}, \|\cdot\|_p)$ with $\iota_1(\underline{h}) := \underline{h}$ and $\iota_2 : (\mathbb{C}^{N_\mathrm{s} \times N_\mathrm{i}}, \|\cdot\|_{\mathrm{Fro}}) \to (\mathbb{C}^{N_\mathrm{s} \times N_\mathrm{i}}, \|\cdot\|_{\mathrm{dis}})$ with $\iota_2(\underline{H}) := \underline{H}$, where $\|\cdot\|_{\mathrm{Fro}}$ is the unweighted Frobenius norm. Clearly, prepending ι_2 and appending ι_1 to the definitions to the discretized forward operator will not change the computed result. The only changes will occur in the adjoint operators, since $\iota_1^*(\underline{g}) = \underline{g}/h_N^d$ and $\iota_2^*(\underline{G}) = \omega^\mathrm{s}\underline{G}$. For example the adjoint of the derivate with respect to the new norms is given by

$$[\underline{\mathcal{F}}'(\underline{q})]^* \underline{H} = \sum_{j=1}^{N_\mathrm{s}} \frac{\omega_j^\mathrm{s}}{h_N^d} \sum_{\ell=1}^{N_\mathrm{i}} \underline{H}_{j,\ell} \, \overline{A_{N_\mathrm{D},N_\mathrm{s}}(j,\cdot)} \, \overline{B_{N_\mathrm{D},N_\mathrm{i}}(\cdot,\ell)} \quad \text{for } \underline{H} \in \mathbb{C}^{N_\mathrm{s} \times N_\mathrm{i}}. \tag{35}$$

The above representations will turn out to be especially helpful for the reconstruction algorithm, cf. Section 4.4, for which repeated evaluations of $\underline{\mathcal{F}}'(\underline{q})[\underline{h}]$ and $[\underline{\mathcal{F}}'(\underline{q})]^*[\underline{\mathcal{F}}(\underline{q})]$ are necessary. We remark that the expensive computation of the matrices $A_{N_\mathrm{D},N_\mathrm{s}} \in \mathbb{C}^{N_S \times N_\mathrm{D}}$ and $B_{N_\mathrm{D},N_\mathrm{i}} \in \mathbb{C}^{N_\mathrm{D} \times N_\mathrm{i}}$ can be set up by solving N_s and N_i forward problems, which makes the full derivative efficiently computable.

3.7 Generation of operators

We finish this section by proposing a possible generation sequence for the discretized operators. To keep the notation simple we consider the three-dimensional space $\mathbb{R}^3$ (i. e., $d = 3$) and even $N \in \mathbb{N}$.

First one chooses six grid parameters: the N_i locations of the sources (point sources or plane waves), the computational domain/region of interest parameters R and N, and the N_s measurement locations x_ℓ^s, $\ell = 1, \ldots, N_\mathrm{s}$ and their type (near of far field measurement).

The region of interest parameters generate two index sets $I = -N/2, \ldots, N/2 - 1$, shifted $I_\mathrm{S} = 0, \ldots, N/2 - 1, -N/2, \ldots, -1$, the grid resolution h_N and volume element h_N^d with $d = 3$, the grid points of the computational domain $x_j^{(N)}$ with $j = (j_1, j_2, j_3)$, $j_1, j_2, j_3 \in I$, see (17), and points of the region of interest x_ℓ for $\ell = 1, \ldots, N_D$, see (22) for N_D. Further, these parameters also determine the operators $\mathcal{E}_N$ and $\mathcal{R}_N$ responsible for the data transport between the computational domain and the region of interest, cf. Section 3.4. These operators can be implemented via a mask marking the region of interest points within the computational domain.

Then, the kind of sources determines the source functions u_j^i, $j = 1, \ldots, N_\mathrm{i}$, as discussed in Section 3.5. The locations of the sources induce then the approximations $\omega^\mathrm{i} \in \mathbb{R}^{N_\mathrm{i}}$ of the infinitesimal element of Γ^i. Consequently the system matrix of the operator $\mathrm{SL}_{N_\mathrm{i},N_\mathrm{D}}$, see (26), is given by $(\omega_j^\mathrm{i} u_j^\mathrm{i}(x_\ell))_{\ell=1,\ldots,N_\mathrm{D},\, j=1,\ldots,N_\mathrm{i}}$. Next, the array $\widehat{\Phi}_N = (\Psi_{2R}(I_\mathrm{S}(j_1), I_\mathrm{S}(j_2), I_\mathrm{S}(j_3)))_{j_1,j_2,j_3=1,\ldots,N}$ is computed which is necessary for the

potential operator $V_{N_\mathrm{D}} : \mathbb{C}^{N_\mathrm{D}} \to \mathbb{C}^{N_\mathrm{D}}$ with $V_{N_\mathrm{D}} \underline{f} = \mathcal{R}_N \mathrm{FFT}_N^{-1} \left[\widehat{\Phi}_N \odot \mathrm{FFT}_N \mathcal{E}_N \underline{f} \right]$, see (23). Its adjoint with respect to the standard inner product is given by $V_{N_\mathrm{D}}^* \underline{f} = \mathcal{R}_N \mathrm{FFT}_N^{-1} \left[\overline{\widehat{\Phi}_N} \odot \mathrm{FFT}_N \mathcal{E}_N \underline{f} \right]$. These operators then determine the Lippmann-Schwinger operator $T_{\underline{q}} = (I - V_{N_\mathrm{D}}(\underline{q} \odot\ ))^{-1}$ and its adjoint with respect to the standard inner product is given by $T_{\underline{q}}^* = (I - V_{N_\mathrm{D}}^*(\overline{\underline{q}} \odot\ ))^{-1}$, see (27). Finally, the measurement type determines the form of the measurement function Φ, see (28) and the paragraph afterwards. The measurement locations x_ℓ^s gives $\omega^\mathrm{s} \in \mathbb{R}^{N_\mathrm{s}}$ the approximations of the infinitesimal element of Γ^s. Together these yield the system matrix of the operator $V_{N_\mathrm{D},N_\mathrm{s}}$, see (29), which is given by $(h_N^d k^2 \Phi(x_\ell - x_j^{(N)}))_{\ell=1,\dots,N_\mathrm{s}, j=1,\dots,N_\mathrm{D}}$. The adjoints of the operators $\mathrm{SL}_{N_\mathrm{i},N_\mathrm{D}}$ and $V_{N_\mathrm{D},N_\mathrm{s}}$ are given by transposing the related system matrices and possibly accounting for weighted norms as discussed at the end of last section.

4 Reconstruction with a primal-dual algorithm

To solve the inverse problem we aim to minimize a Tikhonov functional with adapted penalty terms. For minimization we will employ the primal-dual algorithm (PDA) by Pock, Bischof, Cremers and Chambolle, see [PCBC09] or [CP11, Alg. 1]. Before discussing this algorithm, we introduce important concepts from convex analysis. Readers familiar with this theory might want to omit the next section.

4.1 Subgradient, Fenchel conjugate

The following definitions can be found in [SKHK12, Ch. 2] and [Roc67, Ch. 2]. A functional $f : X \to \mathbb{R} \cup \{+\infty\}$ on a Banach space X is *convex* if $f(\lambda x + (1-\lambda)y) \le \lambda f(x) + (1-\lambda) f(y)$ for all $x, y \in X$ and all $\lambda \in [0,1]$. A convex functional f on X is *lower semi-continuous (l.s.c.)* if the convex level set $\{x \in X : f(x) \le c\}$ is closed for every $c \in \mathbb{R}$.

For a convex functional $f : X \to \mathbb{R} \cup \{\infty\}$ the *effective domain* of f is defined as $\mathrm{dom}(f) := \{x \in X : f(x) < \infty\}$ and f is called *proper* if $\mathrm{dom}(f) \neq \emptyset$. An element x^* of the dual space X^* is a *subgradient* of f at $x \in X$ if the relation $f(y) \ge f(x) + \langle x^*, y - x \rangle$ holds for all $y \in X$. Further, the set of all subgradients of f at x is called the *subdifferential* of f at x and is denoted by

$$\partial f(x).$$

The notions of subgradients and subdifferentials are a generalization of the gradient to (possibly) non-smooth convex functions. In particular, if X is finite-dimensional and f continuously differentiable at x, then the subdifferential $\partial f(x)$ has exactly one element, namely the gradient $\nabla f(x)$. In fact, in that case we do not distinguish between the set and its sole element and write $\partial f = \nabla f$. Finally, for a convex function f on X the *Fenchel conjugate* is defined via

$$f^*(x^*) = \sup_{x \in X} \left[\langle x, x^* \rangle - f(x) \right], \quad x^* \in X^*. \tag{36}$$

Sometimes, in the literature the term "Fenchel dual" or "convex conjugate" is employed for this quantity. It turns out that f^* is convex on the dual space X^*. Further, if f is l.s.c then f^* is l.s.c., too. In a similar way the Fenchel biconjugate is defined via $f^{**}(x) = \sup_{x^* \in X^*} [\langle x, x^* \rangle - f^*(x^*)]$ for $x \in X$. It turns out that the Fenchel conjugation is a bijection between l.s.c. proper convex functions. In particular, for such functions $f = f^{**}$.

4.2 A primal-dual algorithm

In this section we discuss a primal-dual algorithm (PDA) from [CP11, Alg. 1]. To this end, let the two finite-dimensional real vector spaces X, Y be equipped with inner products $\langle \cdot, \cdot \rangle_X$ and $\langle \cdot, \cdot \rangle_Y$ and associated norms and let $K : X \to Y$ be a continuous linear operator with operator norm $\|K\| := \max_{0 \neq x \in X} \frac{\|Kx\|_Y}{\|x\|_X}$.

Problem formulations Let $G : X \to [0, \infty]$ be a proper, convex and l.s.c. functional and $F : X \to [0, \infty)$ convex and l.s.c. The (nonlinear) *primal* problem we want to solve is

$$\min_{x \in X} F(Kx) + G(x). \tag{37}$$

We assume that the Fenchel conjugate $F^* : Y \to [0, \infty]$ of F is proper. Then, replacing $F(z)$ by $F^{**}(z) = \max_{y \in Y}[\langle z, y\rangle - F^*(y)]$ with $z := Kx$ in the primal problem yields the so called *primal-dual* problem

$$\min_{x \in X} \max_{y \in Y} \langle Kx, y\rangle + G(x) - F^*(y), \tag{38}$$

which is an example of a saddle-point problem. Assuming the order of min and max in (38) can be changed without influencing the result and exploiting the fact that $\langle Kx, y\rangle = \langle x, K^*y\rangle$ one obtains the *dual-primal* problem

$$\max_{y \in Y} \min_{x \in X} \langle x, K^*y\rangle - F^*(y) + G(x). \tag{39}$$

Primal-dual algorithm (PDA) The following algorithm was proposed for the solution of the above problems:

Algorithm 4.1 (Primal-dual algorithm (PDA) for convex problems, see [CP11, Alg. 1])**.**

- Initialization: Choose step sizes $\tau, \sigma > 0$, initial vectors $(x^0, y^0) \in X \times Y$ and set $\bar{x}^0 = x^0$.
- Iterations ($n \geq 0$): Update $x^n, y^n, \bar{x}^n$ as follows:

$$\begin{aligned} &1. \quad y^{n+1} = (I + \sigma \partial F^*)^{-1}(y^n + \sigma K \bar{x}^n), \\ &2. \quad x^{n+1} = (I + \tau \partial G)^{-1}(x^n - \tau K^* y^{n+1}), \\ &3. \quad \bar{x}^{n+1} = 2x^{n+1} - x^n. \end{aligned} \tag{40}$$

To motivate this algorithm assume that (38) and (39) have at least one solution $(\hat{x}, \hat{y}) \in X \times Y$, such that 0 belongs to the subdifferential of the functionals in (38) with fixed $x = \hat{x}$ and (39) with fixed $y = \hat{y}$. Then the corresponding extremality conditions are $K\hat{x} \in \partial F^*(\hat{y})$ and $-(K^*\hat{y}) \in \partial G(\hat{x})$. Multiplying both sides of the first condition with $\sigma \neq 0$ and adding $\hat{y}$ we get $\hat{y} + \sigma K\hat{x} \in \hat{y} + \partial F^*(\hat{y})$, which yields the following implicit equation for $\hat{y}$,

$$\hat{y} = (I + \sigma \partial F^*)^{-1}(\hat{y} + \sigma K\hat{x}).$$

Similarly the second condition gives $\hat{x} = (I + \tau \partial G)^{-1}(\hat{x} - \tau K^*\hat{y})$ with $\tau \neq 0$. The primal-dual algorithm connects then alternating fixed-point iterations for $\hat{x}, \hat{y}$ with an extrapolation step. In particular, the above algorithm can be interpreted as a fixed-point iteration with an over-relaxation step in the last line, see [HH14, Sec. 2].

Theorem 4.2 (Convergence of PDA)**.** *We assume that the primal-dual problem* (38) *has a saddle-point* $(\hat{x}, \hat{y})$ *and the step sizes* τ,σ *are such that* $\tau\sigma\|K\|^2 < 1$*. Then there exists a saddle-point* (x^*, y^*)*, such that* $x^n \to x^*$ *and* $y^n \to y^*$ *as* $n \to \infty$*.*

A proof of Theorem 4.2 for real vector spaces can be found in [CP11, Th. 1]. We stress that the real vector spaces are indeed crucial for Algorithm 4.1, as the symmetry of the inner product is exploited in the proof and both subgradient and Fenchel conjugate are real-valued concepts. We will present a related minimization scheme for complex-valued functionals later on in Section 4.5. Further, to compute the inverses in (40) the following characterization turns out to be useful.

Lemma 4.3 (Proximal mapping, resolvent operator, see [BL11, Lemma 6.134])**.** *Let* X *be a real Hilbert space and* $G : X \to \mathbb{R} \cup \{+\infty\}$ *proper, convex and l.s.c. For all* $\tau > 0$ *and all* $w \in X$*,*

$$(I + \tau \partial G)^{-1}(w) = \operatorname*{arg\,min}_{z \in X} \left[\frac{\|z - w\|_X^2}{2} + \tau G(z) \right].$$

In the literature sometimes a distinction is made between the left hand side operator $(I + \tau \partial G)^{-1}$ *and the operator implicitly defined by the right hand side variational problem. The former is called* resolvent operator *while the latter is called* proximal mapping*. Since the assumptions of the lemma will always be fulfilled in our setting we will uniformly use the term proximal mapping.*

Indicator functions The proximal mapping may be viewed as a generalization of the orthogonal projection. To see this, proximal mappings of indicator functions are considered.

Definition 4.4 (Indicator function)**.** For a subset $C \subset X$ of Hilbert space X we define an *indicator function*

$$\delta_C(w) := \begin{cases} 0 & \text{if } w \in C, \\ +\infty & \text{otherwise.} \end{cases}$$

Slightly overloading the notation we define for real-valued vectors w the element-wise indicator function on $[a, b]$,

$$\delta_{[a,b]}(w) := \sum_i \delta_{[a,b]}(w_i). \tag{41}$$

In other words, $\delta_{[a,b]}(w)$ is zero if every element w_i is in interval $[a, b]$, $\delta_{[a,b]}(w)$ is ∞ otherwise.

Remark 4.5. *We recall that the orthogonal projection P_C onto the closed convex set $C \subset X$, see [LMM12, Sec. 2.1], is defined as $P_C(w) = \frac{1}{2} \arg\min_{z \in C} \|z - w\|_X^2$. Clearly, with the help of the indicator function δ_C the projection operator P_C can also be written as an unconstrained minimization problem $P_C(w) = \arg\min_{z \in X} \left[\frac{1}{2}\|z - w\|_X^2 + \tau\delta_C(z)\right]$, with arbitrary $\tau > 0$. However, this is exactly the definition of the proximal mapping for the indicator function.*

4.3 The Tikhonov functional

With the preparations of the last section, we are now ready to state the variational problem and the involved Tikhonov functional essential for the reconstruction of the contrast in the scattering problem. As we are focused on the implementational aspects of the proposed algorithm, we only consider finite-dimensional spaces both for the searched-for contrast and the multi-static measurements. For simplicity, omit to denote this discrete setting explicitly. We also remark that due to the shape of the region of interest the elements of the contrast can be considered a vector or tuple and at the same time a rectangular array. To avoid overloading notation we will avoid to differentiate between these notations, whenever it is clear from the context which one is meant.

Forward operator and his spaces Therefore, we do no longer need to differentiate in the notation between functions and their discretizations. To simplify notation in what follows, we no longer underline discrete quantities. In particular, from now on q shall refer to the discrete version of the contrast and $\mathcal{F}$, $\mathcal{F}'$ to the discretized(!) forward operator and its derivative, see (30) and (32). The forward operator $\mathcal{F}$ is assumed to map between finite-dimensional spaces X and Y_{dis} with

$$\begin{array}{rcll} X & := & \mathbb{C}^{N_{\text{D}}} & \text{equipped with the inner product (33) and} \\ Y_{\text{dis}} & := & \mathbb{C}^{N_{\text{s}} \times N_{\text{i}}} & \text{equipped with the inner product (34).} \end{array} \tag{42}$$

The related norms are denoted as $\|\cdot\|_{\text{roi},2}$ and $\|\cdot\|_{\text{dis}}$. In both cases we identify the dual space of these Hilbert spaces with the spaces themself. Sometimes, in cases where the inner product is not important, we will overload the notation and write $X = \mathbb{C}^{N_{\text{D}}}$ and $Y_{\text{dis}} = \mathbb{C}^{N_{\text{s}} \times N_{\text{i}}}$ to make the dimension of the space explicit.

Discrepancy, Tikhonov functional We assume that a noisy version of the data $F_{\text{meas}}^{\delta} \in Y_{\text{dis}} = \mathbb{C}^{N_{\text{s}} \times N_{\text{i}}}$ is available. We quantify the defect between the data $\mathcal{F}(q)$ and the measured data F_{meas} by the $\|\cdot\|_{\text{dis}}$ norm, $\frac{1}{2}\|\mathcal{F}(q) - F_{\text{meas}}^{\delta}\|_{\text{dis}}^2$. Of course, it is well-known that the minimization of the discrepancy (for fixed measured data and variable q) will in general not yield reasonable reconstructions, see e. g. [DDD04]. To stabilize the process, a convex regularization penalty term $\mathcal{R}$ is added to the discrepancy. In literature, this general paradigm is called variational regularization or Tikhonov regularization. The resulting functional $\frac{1}{2}\|\mathcal{F}(q) - F_{\text{meas}}^{\delta}\|_{\text{dis}}^2 + \alpha\,\mathcal{R}(q)$, is called *Tikhonov functional*. The number $\alpha > 0$ is a regularization parameter. It controls the pay-off between the approximation in the discrepancy and the regularization term, [CP11, Sec. 6.2.1]. In general, the penalty term is chosen to take into account a-priori information on q. In the remainder of this section penalty terms and the related Tikhonov functional are presented, that are sensible in the context of inverse medium problems. In particular, separate regularization parameters for every a-priori information/regularization term will be considered.

A-priori information: sparsity We assume that the contrast array $q \in X = \mathbb{C}^{N_D}$ has only few non-zero entries. In other words it can be represented in the pixel basis with only few non-zero coefficients. This is called *sparsity* (with respect to the pixel basis) and will be enforced in the reconstructions by means of the penalty term, see [SKHK12, Ch. 1.5], $\alpha \|q\|_{\text{spa}}$, where

$$\|x\|_{\text{spa}} := h_N^d \sum_i |\operatorname{Re} x_i| + |\operatorname{Im} x_i|, \quad x \in \mathbb{C}^{N_D},$$

and $\alpha > 0$ is a regularization parameter.

A-priori information: sharp edges In addition to the sparsity assumptions we also assume that the ground truth contrasts exhibit sharp edges. Therefore, we introduce the total variation semi-norm, see [CP11, Sec. 6.2.1], as a further penalty term. We only present the 2D case, as the extension to 3D is straightforward. In particular, in this paragraph the elements of X are interpreted as multi-dimensional arrays. A discretization of the gradient acting on square arrays is defined by

$$(\nabla a)_{i,j} = \begin{pmatrix} (\nabla a)^{(1)}_{i,j} \\ (\nabla a)^{(2)}_{i,j} \end{pmatrix} \quad \text{with } (\nabla a)^{(1)}_{i,j} := \begin{cases} \frac{a_{i+1,j}-a_{i,j}}{h} & \text{if } i < N, \\ 0 & \text{if } i = N, \end{cases} \quad \text{and } (\nabla a)^{(2)}_{i,j} := \begin{cases} \frac{a_{i,j+1}-a_{i,j}}{h} & \text{if } j < N, \\ 0 & \text{if } j = N, \end{cases}$$

where N is the size of the matrix in one direction and h is the size of the underlying grid, cf. [CP11, Sec. 6.1]. The above operators can be efficiently implemented via shift operations. When implementing the proposed algorithm the practitioners should keep in mind that the above definitions differ from the definition of the `gradient` routine in MATLAB, see [Mat].

Next, the total variation (TV) semi-norm is defined,

$$\|\nabla q\|_{\text{tv}} := h_N^2 \sum_{i,j} |(\nabla q)_{i,j}|, \quad \text{with} \quad |(\nabla q)_{i,j}| := \sqrt{|(\nabla q)^{(1)}_{i,j}|^2 + |(\nabla q)^{(2)}_{i,j}|^2}, \qquad \text{(2D case)}, \tag{43}$$

where the factor h_N^2 is due to the two-dimensional volume measure on the region of interest D. (For the 3D case is has to be replaced by h_N^3.) The reader should be aware that, in general, $\|\nabla q\|_{\text{tv}}$ differs from the ℓ^1 norm of ∇q, if ∇q is written as a single vector. To promote sharp edges in the reconstruction the penalty $\beta \|\nabla q\|_{\text{tv}}$, where $\beta > 0$ is an additional regularization parameter, is introduced to the Tikhonov functional.

A-priori information: physical bounds Finally, in general characteristic physical bounds of the values for the contrast are known. We incorporate this information with the indicator functions defined in (41). To this end, we introduce the (convex) functional $\delta_{[a,b]}(\operatorname{Re}(q)) + \delta_{[c,d]}(\operatorname{Im}(q))$, where $a \le b$ and $c \le d$ describe physical bounds for the real and imaginary part. For example, with the assumption $\operatorname{Im}(q) \ge 0$ of the Theorem 3.2 in mind one may consider $c \ge 0$ a sensible choice.

Tikhonov functional, linearization Collecting the functionals from the previous paragraphs yields the problem

$$\min_{q \in X} \tfrac{1}{2} \|\mathcal{F}(q) - F^{\delta}_{\text{meas}}\|^2_{\text{dis}} + \alpha \|q\|_{\text{spa}} + \beta \|\nabla q\|_{\text{tv}} + \delta_{[a,b]}(\operatorname{Re}(q)) + \delta_{[c,d]}(\operatorname{Im}(q)), \tag{44}$$

where $\alpha, \beta > 0$ are regularization parameters. Unfortunately, the functional in (44) involves a nonlinear operator and will therefore in general fail to be convex. To be able to use the PDA of (40) we linearize the problem. Thus, we replace $\mathcal{F}(q)$ by the linearization at q given by $\mathcal{F}(q) + \mathcal{F}'(q)[h]$ and successively minimize

$$\min_{h \in X} \tfrac{1}{2} \|\mathcal{F}'(q)[h] + \mathcal{F}(q) - F^{\delta}_{\text{meas}}\|^2_{\text{dis}} + \alpha \|q + h\|_{\text{spa}} + \beta \|\nabla(q + h)\|_{\text{tv}} + \delta_{[a,b]}(\operatorname{Re}(q + h)) + \delta_{[c,d]}(\operatorname{Im}(q + h)). \tag{45}$$

Alternative discrepancy and penalty terms Of course it is possible to use other discrepancy and penalty terms in (45) respectively (44). For example, for different noise statistics other discrepancy terms could be appropriate, e. g. unweighted Frobenius norm, Schatten norm etc. For the penalty, one could consider the sparsity of the contrast in another system, e. g. a wavelet or other advanced harmonic basis. For example, for wavelets this results in the penalty function $\alpha \|\mathcal{W}(q + h)\|_1$ of h, where $\mathcal{W}$ is the forward wavelet operator. However, in our experiments with the Cohen-Daubechies-Feauveau-9/7 wavelets we obtained slightly worse results than for the presented functionals. Hence, we omit this approach here.

4.4 Proposed iterative reconstruction scheme

The proposed scheme then iteratively interleaves the linearization and variational step. The idea is to improve the current iterate $q^{(m)} \in X$ by a step $h^{(m)} \in X$ that minimizes the functional in (45) for $q = q^{(m)}$ (inner iteration) and update $q^{(m+1)} := q^{(m)} + h^{(m)}$ (outer iteration). This successively computes the linearization of $\mathcal{F}$ at $q^{(m+1)}$. Since the PDA of (45) is formulated for real vector spaces we transform the linearized problem into a minimization problem on a real vector space, i. e. we seek for q in $X_{\mathbb{R}} := \mathbb{R}^{N_{\mathrm{D}}} \times \mathbb{R}^{N_{\mathrm{D}}}$ instead of q in $X := \mathbb{C}^{N_{\mathrm{D}}}$. The details of that step are presented in the next section. In the following we will look at the complete inversion scheme. Then, the remainder of this section is devoted to the motivation of this scheme.

1. Initialization of the outer iteration:
   Set outer iteration number $m = 0$ and initial contrast $q^{(0)} = 0 \in X_{\mathbb{R}} := \mathbb{R}^{N_{\mathrm{D}}} \times \mathbb{R}^{N_{\mathrm{D}}}$.

2. Inner iteration solving the linearized minimization problem (45) employing primal-dual algorithm (PDA):

   (a) Initialization of the inner iteration: Set inner iteration number $n = 0$. Remember $\mathcal{F}(q^{(m)})$ in (30). Compute $A_{N_{\mathrm{D}},N_{\mathrm{s}}}$ and $B_{N_{\mathrm{D}},N_{\mathrm{i}}}$ for fast computation of $\mathcal{F}'(q^{(m)})[h]$ and $[\mathcal{F}'(q^{(m)})]^* H$, see (32) and (35). Choose step sizes $\tau, \sigma > 0$ as in (71). Set $\bar{x}^{[0]} = x^{[0]} = 0 \in X_{\mathbb{R}}$, $y_{\mathrm{dis}}^{[0]} = 0 \in Y_{\mathrm{dis},\mathbb{R}} = \mathbb{R}^{N_{\mathrm{s}} \times N_{\mathrm{i}}} \times \mathbb{R}^{N_{\mathrm{s}} \times N_{\mathrm{i}}}$, and $y_{\mathrm{tv}}^{[0]} = 0 \in Y_{\mathrm{tv},\mathbb{R}} = X_{\mathbb{R}} \times X_{\mathbb{R}}$ (in 2D case) as initial vectors. That means, we consider a tuple $((y^{(1),\mathrm{Re}}, y^{(1),\mathrm{Im}}), (y^{(2),\mathrm{Re}}, y^{(2),\mathrm{Im}})) \in Y_{\mathrm{tv},\mathbb{R}}$. For the definitions of v_{dis}, v_{tv}, K_{dis}, K_{tv} see (52) in combination with (51) and for their adjoints K_{dis}^* and K_{tv}^* see (61).

   (b) Dual step $(\bar{x}^{[n]}, y_{\mathrm{dis}}^{[n]}, y_{\mathrm{tv}}^{[n]}) \;\to\; (\bar{x}^{[n]}, y_{\mathrm{dis}}^{[n+1]}, y_{\mathrm{tv}}^{[n+1]})$ with dual step size $\sigma > 0$:

$$\begin{aligned} w_{\mathrm{y,dis}} &:= y_{\mathrm{dis}}^{[n]} + \sigma K_{\mathrm{dis}}(\bar{x}^{[n]}), \\ y_{\mathrm{dis}}^{[n+1]} &= (I + \sigma F_{\mathrm{dis}}^*)^{-1}(w_{\mathrm{y,dis}}) = \frac{w_{\mathrm{y,dis}} + \sigma v_{\mathrm{dis}}}{1+\sigma}, \end{aligned} \tag{46}$$

$$\begin{aligned} w_{\mathrm{y,tv}} &:= y_{\mathrm{tv}}^{[n]} + \sigma K_{\mathrm{tv}}(\bar{x}^{[n]}), \\ z &:= w_{\mathrm{y,tv}} + \sigma v_{\mathrm{tv}}, \\ (y_{\mathrm{tv}}^{[n+1]})_i^{(k),\ell} &= ((I + \sigma F_{\mathrm{tv}}^*)^{-1}(w_{\mathrm{y,tv}}))_i^{(k),\ell} = \frac{z_i^{(k),\ell}}{\max\{1, |z_i|\}} \end{aligned} \tag{47}$$

$$\text{with } k = 1, \dots, d, \ \ell \text{ is Re or Im, and } |z_i| \text{ as defined in (57).} \tag{48}$$

   (c) Primal step $(x^{[n]}, y_{\mathrm{dis}}^{[n+1]}, y_{\mathrm{tv}}^{[n+1]}) \;\to\; (x^{[n+1]}, y_{\mathrm{dis}}^{[n+1]}, y_{\mathrm{tv}}^{[n+1]})$ with primal step size $\tau > 0$:

$$w_{\mathrm{x}} = x^{[n]} - \tau(K_{\mathrm{dis}}^*(y_{\mathrm{dis}}^{[n+1]}) + K_{\mathrm{tv}}^*(y_{\mathrm{tv}}^{[n+1]})), \tag{49}$$

$$\begin{aligned} \kappa &:= \tau\alpha\, h_N^d, \quad N_{\mathbb{R}} := \{1, \dots, N_{\mathrm{D}}\}, \quad N_{\mathbb{C}} := \{N_{\mathrm{D}}+1, \dots, 2N_{\mathrm{D}}\} \\ x_j^{[n+1]} &= (I + \tau G)^{-1}(w_{\mathrm{x},j}) = -q_j + \begin{cases} \mathcal{I}_{[a,b]}\mathbb{S}_\kappa(w_{\mathrm{x},j} + q_j) & \text{if } j \in N_{\mathbb{R}}, \\ \mathcal{I}_{[c,d]}\mathbb{S}_\kappa(w_{\mathrm{x},j} + q_j) & \text{if } j \in N_{\mathbb{C}}, \end{cases} \\ &= -q_j + \begin{cases} \max\{a, \min\{b, \mathrm{sign}(z)\ \max\{|z| - \kappa, 0\}\}\} \text{ with } z := w_{\mathrm{x},j} + q_j & \text{if } j \in N_{\mathbb{R}}, \\ \max\{c, \min\{d, \mathrm{sign}(z)\ \max\{|z| - \kappa, 0\}\}\} \text{ with } z := w_{\mathrm{x},j} + q_j & \text{if } j \in N_{\mathbb{C}}. \end{cases} \end{aligned} \tag{50}$$

   (d) Extrapolation step: $\bar{x}^{[n+1]} = 2x^{[n+1]} - x^{[n]}$.

   (e) Stop the inner iteration by tolerance-based rules, which we will present in Section 4.10 as outer or inner tolerance principle, and set
   $$h^{(m)} := x^{[n+1]}.$$
   Otherwise set $n := n + 1$ and go to step (2b) again.

3. Outer iteration step:

   (a) $q^{(m+1)} = q^{(m)} + h^{(m)}$ and $m := m + 1$.

   (b) Stop the outer iteration by the discrepancy principle, see Section 4.9. Otherwise go to step 2 again.

4.5 Transformation of the complex problem

In oder to construct the operator K in PDA as an operator between real vector spaces we transform complex-valued quantities by means of the identification of $\mathbb{C}$ as $\mathbb{R}^2$.

Transformation of complex into real vectors Formally, the transport between complex and real-valued form is carried out by the transformations:

$$\begin{array}{rcl} \mathrm{T} & : & \mathbb{C} \to \mathbb{R}\times\mathbb{R}, \qquad \mathrm{T}(x) := (\mathrm{Re}(x),\, \mathrm{Im}(x)), \\ \mathrm{T}^{-1} & : & \mathbb{R}\times\mathbb{R} \to \mathbb{C}, \qquad \mathrm{T}^{-1}(y) = y^{\mathrm{Re}} + \mathrm{i}\, y^{\mathrm{Im}} \quad \text{where} \quad y = (y^{\mathrm{Re}}, y^{\mathrm{Im}}). \end{array} \tag{51}$$

Of course, as usual the above pair extends by element-wise application to vectors, matrices and arrays. For example, $\mathbb{C}^n$ is identified with $\mathbb{R}^n \times \mathbb{R}^n$, where the first $\mathbb{R}^n$ is responsible for the real parts and the second $\mathbb{R}^n$ for the imaginary part. We hasten to stress that in the above definitions the set of complex numbers is considered to be a vector space over the field of real numbers and not (as is usually the case) over the complex numbers. This setting is necessary to ensure that the operators are linear. Formally this can only be the case if the related operator maps between vector spaces over the same field.

Reformulated Tikhonov problem In the next step we formulate the post-linearization problem (45) in real vector spaces. For the remainder of this section we assume that the linearization point q as well the minimization variable h are already in the transported real vector space. Firstly, we define the auxiliary quantities

$$\begin{array}{rclcrcl} K_{\mathrm{dis}} & := & \mathrm{T}[\mathcal{F}'(\mathrm{T}^{-1}q)]\mathrm{T}^{-1}, & & v_{\mathrm{dis}} & := & \mathrm{T}(\mathcal{F}(\mathrm{T}^{-1}q) - F^{\delta}_{\mathrm{meas}}), \\ K_{\mathrm{tv}} & := & \beta\, \mathrm{T}\nabla\mathrm{T}^{-1}, & & v_{\mathrm{tv}} & := & \beta\, \mathrm{T}\nabla\mathrm{T}^{-1}q. \end{array} \tag{52}$$

Secondly, transporting the functionals of (45) into the real vector space $X_{\mathbb{R}} := \mathbb{R}^{N_{\mathrm{D}}} \times \mathbb{R}^{N_{\mathrm{D}}}$ yields the

$$\begin{array}{rl} \text{discrepancy (linearized problem)} & f_{\mathrm{dis}}(h) := \frac{1}{2}\|K_{\mathrm{dis}}h + v_{\mathrm{dis}}\|^2_{\mathrm{dis},\mathbb{R}}, \\ \text{the sparsity penalty} & f_{\mathrm{spa}}(h) := \alpha\|h+q\|_{\mathrm{spa},\mathbb{R}}, \\ \text{the TV-penalty} & f_{\mathrm{tv}}(h) := \|K_{\mathrm{tv}}h + v_{\mathrm{tv}}\|_{\mathrm{tv},\mathbb{R}}, \\ \text{and the penalty for physical bounds} & f_{\mathrm{phy}}(h) := \delta_{[a,b,c,d]}(h+q). \end{array} \tag{53}$$

Roughly, the norms with the subindex $\mathbb{R}$ are real-valued identifications of their complex counterparts, i. e. $\|x\| = \|Tx\|_{\mathbb{R}}$. Of course, in the next step these terms are defined explicitly.

Firstly, due to (42), the transported version of $X_{\mathbb{R}}$ is given by the space

$$X_{\mathbb{R}} := \mathbb{R}^{N_{\mathrm{D}}} \times \mathbb{R}^{N_{\mathrm{D}}}.$$

To equip this space with an inner product we rely on the original inner product of X, cf. (42) and (33),

$$\langle x, y\rangle_{\mathrm{roi},\mathbb{R}} := \mathrm{Re}\langle \mathrm{T}^{-1}x, \mathrm{T}^{-1}y\rangle_{\mathrm{roi}} = h_N^d \sum_i \left(x_i^{\mathrm{Re}} y_i^{\mathrm{Re}} + x_i^{\mathrm{Im}} y_i^{\mathrm{Im}}\right), \quad x, y \in X_{\mathbb{R}}. \tag{54}$$

Of course, this is done so to ensure that the topology on the original and transported space is the same. This ensures especially that the derivatives do not change. Next we define

$$\|x\|_{\mathrm{spa},\mathbb{R}}(x) := h_N^d \sum_i |x_i^{\mathrm{Re}}| + |x_i^{\mathrm{Im}}|, \quad x = (x^{\mathrm{Re}}, x^{\mathrm{Im}}) \in X_{\mathbb{R}} \tag{55}$$

and

$$\delta_{[a,b,c,d]}(x) := \delta_{[a,b]}(x^{\mathrm{Re}}) + \delta_{[c,d]}(x^{\mathrm{Im}}), \quad x = (x^{\mathrm{Re}}, x^{\mathrm{Im}}) \in X_{\mathbb{R}}.$$

In the next step we define $\|\cdot\|_{\mathrm{tv},\mathbb{R}}$. For the sake of simplicity we discuss the 2D case, since the changes necessary for the 3D case are obvious. First we recall that in 2D the $\|\cdot\|_{\mathrm{tv}}$ norm operates on the gradients of vectors from X, i. e. the space $X \times X$. Consequently, the norm $\|\cdot\|_{\mathrm{tv},\mathbb{R}}$ must operate on

$$Y_{\mathrm{tv},\mathbb{R}} := X_{\mathbb{R}} \times X_{\mathbb{R}}.$$

This results in the definition, cf. (43),

$$\|a\|_{\mathrm{tv},\mathbb{R}} := h_N^2 \sum_i |(a_i^{(1),\mathrm{Re}}, a_i^{(1),\mathrm{Im}}, a_i^{(2),\mathrm{Re}}, a_i^{(2),\mathrm{Im}})|, \qquad \text{(2D case)} \tag{56}$$

where of course $((a^{(1),\mathrm{Re}}, a^{(1),\mathrm{Im}}), (a^{(2),\mathrm{Re}}, a^{(2),\mathrm{Im}})) \in Y_{\mathrm{tv},\mathbb{R}}$ and

$$|(a_i^{(1),\mathrm{Re}}, a_i^{(1),\mathrm{Im}}, a_i^{(2),\mathrm{Re}}, a_i^{(2),\mathrm{Im}})|^2 := |a_i^{(1),\mathrm{Re}}|^2 + |a_i^{(1),\mathrm{Im}}|^2 + |a_i^{(2),\mathrm{Re}}|^2 + |a_i^{(2),\mathrm{Im}}|^2 . \tag{57}$$

In the same way as for the space X, we get for Y_{dis}

$$Y_{\mathrm{dis},\mathbb{R}} := \mathbb{R}^{N_\mathrm{s} \times N_\mathrm{i}} \times \mathbb{R}^{N_\mathrm{s} \times N_\mathrm{i}}$$

and the inner product on $Y_{\mathbb{R}}$, cf. (34),

$$\langle x, y \rangle_{\mathrm{dis},\mathbb{R}} := \mathrm{Re} \langle \mathrm{T}^{-1} x, \mathrm{T}^{-1} y \rangle_{\mathrm{dis}}, \quad x, y \in Y_{\mathrm{dis},\mathbb{R}}. \tag{58}$$

All the above elementary, but indispensable, work allows us to identify the three main ingredients of the primal problem (37), the operator K with its pre-image and image space and the functionals F and G. The remainder of the section is devoted to that task.

Operator K and its adjoint We begin with the definition of the related operator K. In our approach it shall be given by

$$K := (K_{\mathrm{dis}}, K_{\mathrm{tv}}),$$

where K_{dis} and K_{tv} are as in (52). All operators involved in the definition of K are $\mathbb{R}$-linear. Therefore the operator K is $\mathbb{R}$-linear too. Of course, some operators are even $\mathbb{C}$-linear, which doesn't bother us here. (Note that T^{-1} is $\mathbb{C}$-linear, but T only $\mathbb{R}$-linear.)

For the sake of the proposed algorithm we also need the exact form of the adjoint of K. Therefore, we need to discuss closely the pre-image space and the image space of K together with their related inner products/norms. After the considerations of the previous paragraph it is clear that the canonical choice for the pre-image space is the space $X_{\mathbb{R}}$. The canonical choice for the image space is the product space $Y := Y_{\mathrm{dis}} \times Y_{\mathrm{tv}}$, since K_{dis} maps into Y_{dis} and K_{tv} maps into Y_{tv}. Of course, instead of the penalty $\|\cdot\|_{\mathrm{tv},\mathbb{R}}$ the space Y_{tv} is equipped with the norm generated by the inner product

$$\langle x, y \rangle_{\mathrm{tv},\mathbb{R}} := \langle x^{(1)}, y^{(1)} \rangle_{\mathrm{roi},\mathbb{R}} + \langle x^{(2)}, y^{(2)} \rangle_{\mathrm{roi},\mathbb{R}}, \quad x, y \in Y_{\mathrm{tv},\mathbb{R}}. \tag{59}$$

Of course, the reader should be aware that the norm induced by that inner product is not the functional $\|\cdot\|_{\mathrm{tv},\mathbb{R}}$ in (56). The indices "tv" were chosen in both cases to indicate on which objects both quantities act.

In a similar way to (59) the inner product on Y is generated by

$$\langle (y_{\mathrm{dis}}, y_{\mathrm{tv}}), (z_{\mathrm{dis}}, z_{\mathrm{tv}}) \rangle_Y := \langle y_{\mathrm{dis}}, z_{\mathrm{dis}} \rangle_{\mathrm{dis},\mathbb{R}} + \langle y_{\mathrm{tv}}, z_{\mathrm{tv}} \rangle_{\mathrm{tv},\mathbb{R}} \tag{60}$$

with the inner products (58) and (59). Altogether

$$K : X_{\mathbb{R}} \to Y_{\mathrm{dis},\mathbb{R}} \times Y_{\mathrm{tv},\mathbb{R}}.$$

The pre-image and image space are both Hilbert spaces and we identify their duals with the spaces themselves. Since

$$\langle Kh, y \rangle_Y = \langle (K_{\mathrm{dis}} h, K_{\mathrm{tv}} h), (y_{\mathrm{dis}}, y_{\mathrm{tv}}) \rangle_Y = \langle h, K_{\mathrm{dis}}^* \, y_{\mathrm{dis}} \rangle_{\mathrm{roi},\mathbb{R}} + \langle h, K_{\mathrm{tv}}^* \, y_{\mathrm{tv}} \rangle_{\mathrm{roi},\mathbb{R}},$$

the adjoint of K is given by

$$K^* : Y_{\mathrm{dis},\mathbb{R}} \times Y_{\mathrm{tv},\mathbb{R}} \to X_{\mathbb{R}}, \quad K^*(y_{\mathrm{dis}}, y_{\mathrm{tv}}) = K_{\mathrm{dis}}^*(y_{\mathrm{dis}}) + K_{\mathrm{tv}}^*(y_{\mathrm{tv}}) . \tag{61}$$

To determine the explicit form of K_{dis}^* one connects the definition of $K_{\mathrm{dis}} = \mathrm{T}[\mathcal{F}'(\mathrm{T}^{-1}q)]\mathrm{T}^{-1}$, see (52), with the efficient evaluation of $[\mathcal{F}'(q)]^*$, see (32) and (35). For K_{tv}^*, on the other hand, one has to consider the adjoint

of the discrete gradient operator, which is the discrete divergence operator because of $\langle \nabla a, b\rangle_Y = -\langle a, \operatorname{div} b\rangle_X$, see [CP11, Sec. 6.1]. For the sake of brevity we present the form of div for 2D case only, the 3D holds mutatis mutandis. For arrays of size N (with underlying grid size h) the 2D version of div is given by

$$\operatorname{div} b = (\operatorname{div} b)^{(1)} + (\operatorname{div} b)^{(2)},$$

where

$$(\operatorname{div} b)^{(1)} := \begin{cases} b^{(1)}_{1,j}/h & \text{if } i = 1, \\ (b^{(1)}_i + b^{(1)}_{i-1,j})/h & \text{if } 1 < i < N, \\ -b_{N-1,j}/h & \text{if } i = N, \end{cases} \qquad (\operatorname{div} b)^{(2)} := \begin{cases} b^{(2)}_{i,1}/h & \text{if } j = 1, \\ (b^{(2)}_i + b^{(2)}_{i,j-1})/h & \text{if } 1 < j < N, \\ -b_{i,N-1}/h & \text{if } j = N. \end{cases}$$

Remark 4.6 (Compatibility of adjoint K^*)**.** *We defined $\mathcal{F}'(q)$ and its adjoint $[\mathcal{F}'(q)]^*$ in a complex vector space, see* (31) *and* (35)*, but consider K in real vector space. We show the compatibility of the adjoint K^* before and after identification of $\mathbb{C}$ with $\mathbb{R}\times\mathbb{R}$ via the operator* T*. Therefore we consider the operator $K_\mathbb{C} := (K_{\mathrm{dis},\mathbb{C}}, K_{\mathrm{tv},\mathbb{C}})$ with $K_{\mathrm{dis},\mathbb{C}} = \mathcal{F}'(q)$ and $K_{\mathrm{tv}} = \beta\nabla$. (Note that this operator is $\mathbb{C}$-linear in comparison to the corresponding K, that is only $\mathbb{R}$-linear.) For this remark we will consider in general $K_\mathbb{C} = \operatorname{Re} K_\mathbb{C} + \mathrm{i}\operatorname{Im} K_\mathbb{C}$ and the complex vector $q = \operatorname{Re} q + \mathrm{i}\operatorname{Im} q$:*

$$K_\mathbb{C}\, q = (\operatorname{Re} K_\mathbb{C} + \mathrm{i}\operatorname{Im} K_\mathbb{C})(\operatorname{Re} q + \mathrm{i}\operatorname{Im} q) = \operatorname{Re} K_\mathbb{C}\operatorname{Re} q + \mathrm{i}\operatorname{Im} K_\mathbb{C}\operatorname{Re} q + \mathrm{i}\operatorname{Re} K_\mathbb{C}\operatorname{Im} q - \operatorname{Im} K_\mathbb{C}\operatorname{Im} q,$$

$$\mathrm{T}[K_\mathbb{C}\, q] = \underbrace{\begin{pmatrix} \operatorname{Re} K_\mathbb{C} & -\operatorname{Im} K_\mathbb{C} \\ \operatorname{Im} K_\mathbb{C} & \operatorname{Re} K_\mathbb{C} \end{pmatrix}}_{=:K_\mathbb{R}} \begin{pmatrix} \operatorname{Re} q \\ \operatorname{Im} q \end{pmatrix} = K_\mathbb{R}[\mathrm{T}q].$$

Finally, we show for a complex vector w that

$$\begin{aligned} \langle K_\mathbb{C}\, q, w\rangle_\mathbb{C} &= \sum_i (K_\mathbb{C}\, q)_i\, \overline{w}_i = \sum_i \sum_j K_{\mathbb{C}_{i,j}}\, q_j\, \overline{w}_i \\ &= \sum_j \sum_i q_j\, K_{\mathbb{C}_{i,j}}\, \overline{w}_i = \sum_j \sum_i q_j\, \overline{K^*_{\mathbb{C}_{j,i}}}\, \overline{w}_i = \sum_j q_j\, (\overline{K^*_\mathbb{C}\, w})_j = \langle q, K^*_\mathbb{C}\, w\rangle_\mathbb{C}. \end{aligned}$$

Note that we used $\overline{K^*_{\mathbb{C}_{j,i}}} = \overline{\overline{K_{\mathbb{C}_{i,j}}}} = K_{\mathbb{C}_{i,j}}$ in the last equation.

Functionals F and G Remembering (53), in the next step we are ready to identify the functionals F and G of the primal problem (37) as

$$F(Kh) = f_{\mathrm{dis}}(h) + f_{\mathrm{tv}}(h), \quad G(h) = f_{\mathrm{spa}}(h) + f_{\mathrm{phy}}(h). \tag{62}$$

Consequently, F splits into two terms

$$F(y_{\mathrm{dis}}, y_{\mathrm{tv}}) := F_{\mathrm{dis}}(y_{\mathrm{dis}}) + F_{\mathrm{tv}}(y_{\mathrm{tv}}), \quad F_{\mathrm{dis}}(y) := \tfrac{1}{2}\|y + v_{\mathrm{dis}}\|^2_{\mathrm{dis},\mathbb{R}}, \quad F_{\mathrm{tv}}(y) := \|y + v_{\mathrm{tv}}\|_{\mathrm{tv},\mathbb{R}}, \tag{63}$$

where $y_{\mathrm{dis}} \in Y_{\mathrm{dis},\mathbb{R}}$, $y_{\mathrm{tv}} \in Y_{\mathrm{tv},\mathbb{R}}$ and $v_{\mathrm{tv}}, v_{\mathrm{dis}}$ are as in (52).

We remark that the above identification of K, F, G is not the only possible. However, it turned out to be especially favorable numerically in our experiments. To implement the PDA we need the explicit form of the mappings $(I + \sigma\partial F^*)^{-1}$ and $(I + \tau\partial G)^{-1}$ for the proposed functionals F and G. The next two sections are devoted to that subject.

4.6 The operator $(I + \sigma\partial F^*)^{-1}$

In this section we determine the form of the proximal mapping of F^* necessary for Algorithm 4.1. First we remark that both the Fenchel conjugate F^* and the subgradient ∂F^* are well-defined, since we consider finite-dimensional real vector spaces. Next we determine the explicit form of the Fenchel conjugate. The form $F(y_{\mathrm{dis}}, y_{\mathrm{tv}}) = F_{\mathrm{dis}}(y_{\mathrm{dis}}) + F_{\mathrm{tv}}(y_{\mathrm{tv}})$ of the functional F, cf. end of last section, implies that $F^*(y_{\mathrm{dis}}, y_{\mathrm{tv}}) = F^*_{\mathrm{dis}}(y_{\mathrm{dis}}) + F^*_{\mathrm{tv}}(y_{\mathrm{tv}})$ where still $y_{\mathrm{dis}} \in Y_{\mathrm{dis},\mathbb{R}}$ and $y_{\mathrm{tv}} \in Y_{\mathrm{tv},\mathbb{R}}$. To see this consider the following lemma:

Lemma 4.7 (Sum of Fenchel conjugates, [RW98, Prop. 11.22]). *Let Y_1 and Y_2 be finite-dimensional real Hilbert spaces, with $Y_1^* = Y_1$, $Y_2^* = Y_2$, further, $Y := Y_1 \times Y_2$ be equipped with the inner product $\langle x, y\rangle_Y = \langle x_1, y_1\rangle_{Y_1} + \langle x_2, y_2\rangle_{Y_2}$ where $x = (x_1, x_2) \in Y$, $y = (y_1, y_2) \in Y$ and, finally, F_1, F_2 be convex functionals. If $F(y) = F(y_1, y_2) := F_1(y_1) + F_2(y_2)$ for all $y \in Y$, then $F^*(y) = F^*(y_1, y_2) = F_1^*(y_1) + F_2^*(y_2)$ for all $y \in Y$.*

Proof. Recalling the definition of the Fenchel conjugate and

$$\begin{aligned} F^*(y_1, y_2) &= \sup\left[\langle (y_1, y_2), (x_1, x_2)\rangle_{Y_1\times Y_2} - F(y_1, y_2) : (x_1, x_2) \in Y_1 \times Y_2\right] \\ &= \sup\left[\langle y_1, x_1\rangle_{Y_1} + \langle y_2, x_2\rangle_{Y_2} - F_1(x_1) - F_2(x_2) : x_1 \in Y_1, x_2 \in Y_2\right] \\ &= \sup\left[\langle y_1, x_1\rangle_{Y_1} - F_1(x_1) : x_1 \in Y_1\right] + \sup\left[\langle y_2, x_2\rangle_{Y_2} - F_2(x_2) : x_2 \in Y_2\right] = F_1^*(y_1) + F_2^*(y_2) \end{aligned}$$

proves the claim. □

Remark 4.8. *Clearly, the above element-wise split implies that the proximal mapping splits too,*

$$(I + \sigma\partial F^*)^{-1}(y_1, y_2) = ((I + \partial F_1^*)^{-1}(y_1), (I + \partial F_2^*)^{-1}(y_2)).$$

Then, the decomposition of F^* together with the definition of Y implies $(I + \sigma\partial F^*)^{-1}(y_{\text{dis}}, y_{\text{tv}}) = ((I + \partial F_{\text{dis}}^*)^{-1}(y_{\text{dis}}), (I + \partial F_{\text{tv}}^*)^{-1}(y_{\text{tv}}))$. Consequently, we need to determine the proximal mappings of F_{dis} and F_{tv}. Further, one recalls that for shift function $f(y) = g(y + b)$ one has $f^*(y) = g^*(y) - \langle b, y\rangle$, see [BL06, Tab. 3.2]. Therefore

$$f(y) = g(y + b) \quad \text{implies} \quad (I + \sigma\partial f^*)^{-1}(y) = (I + \sigma\partial g^*)^{-1}(y + \sigma b)\,. \tag{64}$$

Proximal mapping of F_{dis} To compute the proximal mapping of F_{dis}, see (63), we have $(I+\sigma\partial F_{\text{dis}}^*)^{-1}(y) = (I + \sigma\partial(\frac{1}{2}\|\cdot\|_{\text{dis},\mathbb{R}}^2)^*)^{-1}(y + \sigma v_{\text{dis}})$. For Hilbert norms the functional $\frac{1}{2}\|\cdot\|^2$ has as the Fenchel dual the same term but with dual norm. Therefore the derivative of the Fenchel dual is the identity in the dual space. In our case this means that $(\frac{1}{2}\|\cdot\|_{\text{dis},\mathbb{R}}^2)^* = \frac{1}{2}\|\cdot\|_{\text{dis},\mathbb{R}}^2$ and therefore $\partial(\frac{1}{2}\|\cdot\|_{\text{dis},\mathbb{R}}^2)^* = I$, since $Y_{\text{dis},\mathbb{R}}$ was identified with its dual. Therefore

$$(I + \sigma\partial F_{\text{dis}}^*)^{-1}(y) = \frac{y + \sigma v_{\text{dis}}}{1 + \sigma}, \tag{65}$$

with v_{dis} as in (52).

Proximal mapping of F_{tv} For the proximal mapping of F_{tv} we can again invoke (64) which gives $(I + \sigma\partial F_{\text{tv}}^*)^{-1}(y) = (I + \sigma\partial(\|\cdot\|_{\text{tv},\mathbb{R}})^*)^{-1}(y + \sigma v_{\text{dis}})$. Next, we remember $y \in Y_{\text{tv},\mathbb{R}}$, the notation in (56), and define tuples $y_i \in Y_i$ via $Y_{\text{tv},\mathbb{R}} = Y_1 \times \ldots \times Y_{N_{\text{D}}}$ and

$$y_i := (y_i^{(1),\text{Re}}, y_i^{(1),\text{Im}}, y_i^{(2),\text{Re}}, y_i^{(2),\text{Im}}), \quad \text{(2D case)}, \tag{66}$$

with the obvious modification for the 3D case. Then, the functional $\|\cdot\|_{\text{tv},\mathbb{R}}$, see (56), splits into a sum of terms of the form $h_N^d|y_i|$ with $y_i \in Y_i$ and norm $|\cdot|$ as defined in (57). Consequently, Remark 4.8 applies in extension and implies that the proximal mapping of $(\|\cdot\|_{\text{tv},\mathbb{R}})^*$ can be discussed for the tuples separately.

Remembering that Y is equipped with an inner product, see Section 4.2, we have to look for the Fenchel conjugate to the induced norm by the inner product corresponding to Y_i, i. e. using (59) and (54),

$$\langle x_i, y_i\rangle_{Y_i} = h_N^d\langle x_i, y_i\rangle_2.$$

The induced norm is $\|x\|_{Y_i} = (h_N^d)^{1/2}|x|$, where x means a tuple x_i.

This means, we look for the Fenchel conjugate of $h_N^d\|y_i\|_2 = (h_N^d)^{1/2}(h_N^d)^{1/2}|x| = (h_N^d)^{1/2}\|x\|_{Y_i} = a\,\|\cdot\|$ with $a = (h_N^d)^{1/2}$ and $\|\cdot\| = \|x\|_{Y_i}$ corresponding to the inner product $\langle\cdot,\cdot\rangle_{Y_i}$.

To this end, we see that the proximal mapping $(a\,\|\cdot\|)$ is the orthogonal projection onto the ball with radius a onto the pre-dual norm of $\|\cdot\|$, if the dual pairing between the pre-dual and the norm itself is the same as the inner product used for the orthogonal projection and the inner product used in the definition of the Fenchel conjugate (36). To see this denote $\|\cdot\|_*$ the pre-dual norm. Then $a\,\|x\| = \sup_{\|x^*\|_*\le 1}\langle ax^*, x\rangle = \sup_{\|x^*\|\le a}\langle x^*, x\rangle = \sup\langle x^*, x\rangle - \delta_C(x^*)$, where $C = \{x^* : \|x^*\|_* \le a\}$. A close inspection of (36) reveals that

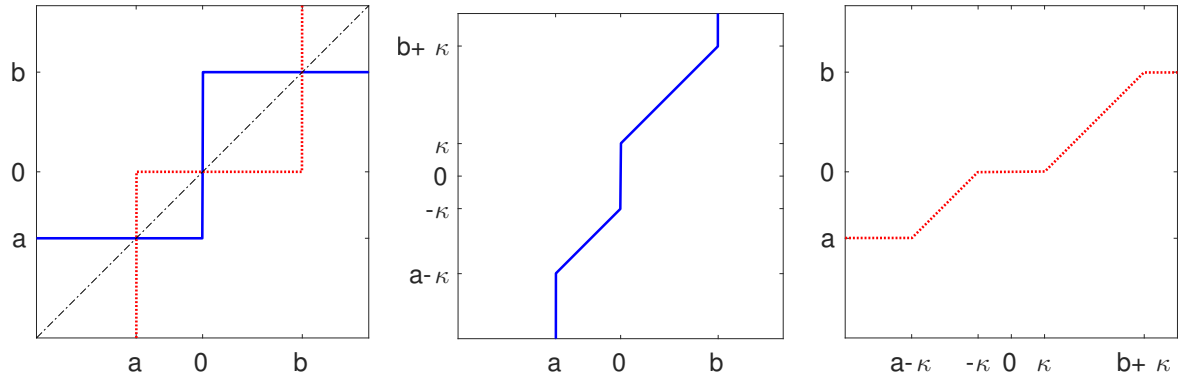

(a) $\mathrm{step}_{[a,b]}$ (blue solid) and $\mathrm{step}^{-1}_{[a,b]}$ (red dotted). (b) $I + \tau\partial g$ (c) $(I + \tau\partial g)^{-1}$

Figure 5: Illustration of $\mathrm{step}_{[a,b]}$ (blue solid) and $\mathrm{step}^{-1}_{[a,b]}$ (red dotted) in (a). We consider $g(x) = \alpha h_N^d |x| + \delta_{[a,b]}(x)$ for $x \in \mathbb{R}$, keep in mind that $\tau\,\mathrm{step}^{-1}_{[a,b]}(x) = \mathrm{step}^{-1}_{[a,b]}(x)$ and plot $(I + \tau\partial g)(x) = x + \kappa\,\mathrm{step}_{[-1,1]}(x) + \mathrm{step}^{-1}_{[a,b]}(x)$ with $\kappa = \tau\,\alpha\,h_N^d$ in (b). The inverse $(I + \tau\partial g)^{-1}$ is the proximal mapping and illustrated in (c).

δ_C is the Fenchel conjugate of $(a\,\|\cdot\|)$. Remark 4.5 then gives the claim. Of course this projection can be explicitly expressed by $x/\max(1, \|x\|_*/a)$, respectively componentwise $x_i/\max(1, \|x\|_*/a)$.

In our case the inner product is as mentioned $\langle x_i, y_i\rangle_{Y_i} = h_N^d \langle x_i, y_i\rangle_2$, see above. Clearly since the norm in the term $(a\|\cdot\|)$ is exactly the norm induced by the inner product, its pre-dual is the norm itself, i. e.

$$\|x\|_*/a = \|x\|_{Y_i}/(h_N^d)^{1/2} = (h_N^d)^{1/2}|x|/(h_N^d)^{1/2} = |x|.$$

Together with the previous considerations this yields for F_{tv} componentwise

$$((I + \sigma F_{\mathrm{tv}}^*)^{-1}(y))_i^{(k),\ell} = \frac{y_i^{(k),\ell} + \sigma(v_{\mathrm{tv}})_i^{(k),\ell}}{\max\{1, |y_i + \sigma(v_{\mathrm{tv}})_i)|\}}, \tag{67}$$

where the norm $|\cdot|$ is as defined in (57) and v_{tv} as in (52), the indexing is in parallel to (66), $k = 1, \ldots, d$, and ℓ is Re or Im.

4.7 The operator $(I + \tau\partial G)^{-1}$

After having computed the proximal mapping for F^* we now direct our attention to the proximal mapping of G, which is needed for the second step of Algorithm 4.1. To this end, one observes that G separates in an element-wise sum with terms of the form $\alpha h_N^d |x^{\mathrm{Re}} + v^{\mathrm{Re}}| + \delta_{[a,b]}(x^{\mathrm{Re}} + v^{\mathrm{Re}})$ and $\alpha h_N^d |x^{\mathrm{Im}} + v^{\mathrm{Im}}| + \delta_{[c,d]}(x^{\mathrm{Im}} + v^{\mathrm{Im}})$, where $x^{\mathrm{Re}}, x^{\mathrm{Im}}, v^{\mathrm{Re}}, v^{\mathrm{Im}}$ are real-valued, see (62) and (55). By the same argumentation that led to Lemma 4.7 and Remark 4.8 the proximal mapping of G splits into element-wise proximal mappings of the terms of the previous two forms. Since both term kinds are structurally similar we consider the first one only.

First, we observe, complementary to (64), if $f(x) = g(x+v)$ then $(I+\tau\partial f)^{-1}(x) = (I+\tau\partial g)^{-1}(x+v) - v$. Therefore, we consider the subgradient of $g(x) := \alpha h_N^d |x| + \delta_{[a,b]}(x)$. To this end, the auxiliary, set-valued step function $\mathrm{step}_{[a,b]}$ and their inverse $\mathrm{step}^{-1}_{[a,b]}$, both illustrated in Fig. 5(a), defined by

$$\mathrm{step}_{[a,b]}(x) := \begin{cases} a & \text{if } x \le 0, \\ [a,b] & \text{if } x = 0, \\ b & \text{if } x \ge 0, \end{cases} \quad \text{and} \quad \mathrm{step}^{-1}_{[a,b]}(x) := \begin{cases} (-\infty, 0] & \text{if } x = a, \\ 0 & \text{if } x \in (a,b), \\ [0,\infty) & \text{if } x = b, \\ \emptyset & \text{otherwise, i. e. } x \notin [a,b], \end{cases}$$

turns out to be useful. An elementary computation, see [DDD04], shows that the subgradient of the first term is given by $\partial(\alpha\,h_N^d\,|x|) = \alpha\,h_N^d\,\mathrm{step}_{[-1,1]}(x)$. Further computation confirms that the subgradient of the

second term is given by $\partial(\delta_{[a,b]}(x)) = \mathrm{step}^{-1}_{[a,b]}(x)$. As can be seen in Fig. 5(c) the inverse of $I + \tau\partial g$ exists. To express it we introduce two operators: the *interval projection* is defined for real-valued x and $a \geq b$ by

$$\mathcal{I}_{[a,b]}(x) := \begin{cases} a & \text{if } x < a, \\ x & \text{if } x \in [a,b], \\ b & \text{if } x > b, \end{cases} \tag{68}$$

and the *soft-shrinkage operator*, see [DDD04], is defined for real-valued x and $a \geq 0$ by

$$\mathbb{S}(x,a) := \begin{cases} x + a & \text{if } x \leq -a, \\ 0 & \text{if } x \in (-a,+a), \\ x - a & \text{if } x \geq a. \end{cases} \tag{69}$$

Of course, for both operators, element-wise application is assumed if x is a vector. In any case the interval projection can be implemented by $\mathcal{I}_{[a,b]}(x) = \max\{a, \min\{b, x\}\}$, whereas the shrinkage operator can be implemented by $\mathbb{S}(x,a) = \mathrm{sign}(x)\,\max\{|x| - a, 0\}$. Then one can write $(I + \tau\partial g)^{-1}(x) = \mathcal{I}_{[a,b]}(\mathbb{S}(x, \tau\alpha h_N^d))$. Accommodating for the shift $+v$ in the original terms results in the following formula for $(I + \tau\partial G)^{-1}(x)$:

$$\begin{array}{rcl} ((I + \tau\partial G)^{-1}(x))^{\mathrm{Re}} & = & \mathcal{I}_{[a,b]}(\mathbb{S}(x^{\mathrm{Re}} + v^{\mathrm{Re}}, \tau\alpha h_N^d)) - v^{\mathrm{Re}}, \\ ((I + \tau\partial G)^{-1}(x))^{\mathrm{Im}} & = & \mathcal{I}_{[c,d]}(\mathbb{S}(x^{\mathrm{Im}} + v^{\mathrm{Im}}, \tau\alpha h_N^d)) - v^{\mathrm{Im}}. \end{array} \tag{70}$$

4.8 Norm estimation and choice of step sizes

The reconstruction scheme proposed in Section 4.4 converges if the step sizes τ and σ are chosen such that $\tau\sigma\|K\|^2 < 1$. The norm of $\|K\|^2$ is given by $\|K\|^2 = \max_{0 \neq x \in X} \frac{\|Kx\|_Y^2}{\|x\|_{\mathrm{roi},2}}$, where the Hilbert norm on Y is as induced by the inner product (60), see (52). It is possible to estimate the norm of K by breaking it down to the norm of the involved operators. However, this rough estimate turned out to be too inefficient for our purposes. Of course, one can proceed to reformulate the problem in spaces with standard inner product, which then enables to employ power iteration for the estimation of the biggest eigenvalue. For our purposes it sufficed to test the operator with a sample of vectors of two kinds, i. e., random vectors, and vectors of the form $(1, \ldots, 1, 0, \ldots, 0)$. (We omit to use all unit basis vectors because they deliver a much too low estimate.) This coarse estimate was then multiplied by a safety factor, in general equal to 2. Empirically, in our experience, if $\|K\|^2$ was estimated too low the proposed PDA diverged sometimes evidently.

In our experiments the choice of step sizes

$$\sigma = \tau \quad \text{both slightly smaller than} \quad \|K\|^{-1} \tag{71}$$

yielded the best results. Because a less severe condition than (71) is sufficient to guarantee convergence, an adaptive step size choice proposed in [BH15, Sec. 2.2] is possible. We tested this choice in our numerical examples, but the requirement for activation was not satisfied.

4.9 Stopping the outer iteration

Recall from Subsection 4.4 that the iterative reconstruction scheme consists of outer iterations, responsible for re-linearization of the forward problem, as well as inner iterations, responsible for update/minimization step within a linearized problem. In general, for the strict analysis of this approach one needs to assume that an infinite number of re-linearizations (outer iteration) and an infinite number of minimization steps (inner iteration) within each linearized minimization problem has been carried out. Clearly, this approach is computationally not feasible. To provide an efficient reconstruction scheme the number of outer and inner iteration steps has to be restricted. To that end, we discuss stopping strategies for the outer and the inner iteration.

To construct an efficient reconstruction scheme we propose to employ *Morozov's discrepancy principle* as the stopping criterion for the outer iteration. Let $m = 1, \ldots, N_{\mathrm{out}}$ be the index of the outer iteration, then

that iteration is stopped after iteration $m = N_{\text{out}}$ if the *relative discrepancy*,

$$\text{dis}(m) := \frac{\|\mathcal{F}(q^{(m)}) - F^{\delta}_{\text{meas}}\|_{\text{dis}}}{\|F^{\delta}_{\text{meas}}\|_{\text{dis}}},$$

is for the first time less than a tolerance $\tau_{\text{dis}} > 1$ times the relative noise level $\delta > 0$,

$$\begin{aligned} &\|\mathcal{F}(q^{(N_{\text{out}})}) - F^{\delta}_{\text{meas}}\|_{\text{dis}} \leq \tau_{\text{dis}}\, \delta\, \|F^{\delta}_{\text{meas}}\|_{\text{dis}} \\ &\qquad \text{whilst } \|\mathcal{F}(q^{(m)}) - F^{\delta}_{\text{meas}}\|_{\text{dis}} > \tau_{\text{dis}}\, \delta\, \|F^{\delta}_{\text{meas}}\|_{\text{dis}} \text{ for } m = 0, \ldots, N_{\text{out}} - 1. \end{aligned} \tag{72}$$

In our numerical examples satisfactory results were achieved for the choice $\tau_{\text{dis}} = 2.5$.

4.10 Stopping the inner iteration

In analogy to the previous section, let the index of the inner iterations with m-th outer iteration be given by $n = 1, \ldots, N_{\text{in}}^{(m)}$. We then propose the following three stopping strategies for the inner iteration.

Constant iteration number A straight forward stopping is given after a fixed number of inner iterations. In our experience, the choice $N_{\text{in}}^{(m)} = 50$ for all outer iterations turned out to be sufficient to robustly and reasonably update the linearized problem.

Stopping strategy 1 The next strategy assumes that an a-priori choice for the number of inner iterations in the m-th outer iteration step was made. We denote this choice by $N_{\text{in}}^{(m)}$. After this number of inner iteration steps was computed this choice is a-posteriori evaluated. We consider the choice "good", if the difference between the linearized and original problem gives approximately the same difference. To quantify this we consider the linearized discrepancy $\text{dis}_{\text{lin}} := \|\mathcal{F}'(q^{(m)})[h^{(m)}] + \mathcal{F}(q^{(m)}) - F^{\delta}_{\text{meas}}\|_{\text{dis}} / \|F^{\delta}_{\text{meas}}\|_{\text{dis}}$ and the non-linearized discrepancy $\text{dis}_{\text{nonlin}} := \|\mathcal{F}(q^{(m)} + h^{(m)}) - F^{\delta}_{\text{meas}}\|_{\text{dis}} / \|F^{\delta}_{\text{meas}}\|_{\text{dis}}$, where $q^{(m)}, h^{(m)}$ are the results of the inner iteration. To keep the notation simple, we omitted the iteration index for both discrepancies. Then, the number of inner iteration steps is considered "good" if the quotient

$$\text{dis}_{\text{rel}} := \text{dis}_{\text{lin}} / \text{dis}_{\text{nonlin}}$$

is approximately 1. Only in that case a higher number of inner iterations "pays off" with respect to the reconstruction quality. Consequently, the number of inner iterations is then updated via

$$N_{\text{in}}^{(m+1)} = \begin{cases} \lceil \mu_{\uparrow}\, N_{\text{in}}^{(m)} \rceil & \text{if } \text{dis}_{\text{rel}} \in (1 - \tau_{\text{out}}, 1 + \tau_{\text{out}}), \\ \lfloor \mu_{\downarrow}\, N_{\text{in}}^{(m)} \rfloor & \text{otherwise} \end{cases}$$

with $\mu_{\uparrow} = 1 + \sqrt{1/m}\, \ln(m)$ and $\mu_{\downarrow} = (\min\{1/\text{dis}_{\text{rel}}, \text{dis}_{\text{rel}}\})^2$. In our experiments the outer tolerance τ_{out} was set to 0.05. Since the above update tends to be too optimistic in the first outer steps, we start with the conservative choice $N_{\text{in}}^{(1)} = 1$. The number of inner iteration is additionally limited to 250 for all outer iteration steps.

Stopping strategy 2 We also propose a stopping strategy which controls the number of necessary inner iteration steps from within the inner iteration. Our idea follows the inexact stopping rule for a Newton-like method, cf. [Rie03, Ch. 7.5.3]. Similar to the previous strategy, the idea is to compute the quotient $\text{dis}_{\text{lin}}/\text{dis}_{\text{nonlin}}$ after each inner iteration. To keep the computational effort moderate, however, the non-linearized discrepancy is fixed within the inner iteration $\text{dis}_{\text{nonlin}} := \|\mathcal{F}(q^{(m)} + h^{(m)}) - F^{\delta}_{\text{meas}}\|_{\text{dis}} / \|F^{\delta}_{\text{meas}}\|_{\text{dis}}$, where $q^{(m)}, h^{(m)}$ are again the results of the last outer iteration step. The linearized discrepancy is then reevaluated after every inner iteration step $\text{dis}_{\text{lin}}^{(n)} := \|\mathcal{F}'(q^{(m)})[h^{(n)}] + \mathcal{F}(q^{(m)}) - F^{\delta}_{\text{meas}}\|_{\text{dis}} / \|F^{\delta}_{\text{meas}}\|_{\text{dis}}$, where $h^{(n)}$ is the current iterate within the inner iteration. The inner iteration is stopped if $\text{dis}_{\text{lin}}^{(n)}/\text{dis}_{\text{nonlin}} < \Theta_m$ for some inner tolerance $\Theta_m \in (0, 1]$. The inner tolerances Θ_m are computed via the following algorithm.

Algorithm 4.9 (Compute inner tolerances Θ_m)**.** Set $\Theta_{\text{start}} \in (0,1)$, $\Theta_{\max} \in (\Theta_{\text{start}}, 1)$, and $\gamma_{\text{tol}} \in (0,1]$. For $m = 1, 2$ set auxiliary tolerances $\tilde{\Theta}_m = \Theta_{\text{start}}$ and compute, for $m \geq 3$,

$$\tilde{\Theta}_m = \begin{cases} 1 - (1 - \Theta_{m-1})\, N_{\text{in}}^{(m-2)} / N_{\text{in}}^{(m-1)} & \text{if } N_{\text{in}}^{(m-1)} \geq N_{\text{in}}^{(m-2)}, \\ \gamma_{\text{tol}}\, \Theta_{m-1} & \text{otherwise,} \end{cases}$$

where $N_{\text{in}}^{(m-2)}$ and $N_{\text{in}}^{(m-1)}$ are the number of steps in the inner iteration for the two previous outer iteration steps. Finally, set

$$\Theta_m = \Theta_{\max} \max\left\{ \tau\, \delta / \text{dis}_{\text{nonlin}}^{(m)}, \tilde{\Theta}_m \right\}, \quad m \in \mathbb{N}.$$

As previously, since inner iterations should contribute to the overall reconstruction, the maximal number of inner iterations is capped to 250. Further, in our experiments the parameters were set to $\Theta_{\text{start}} = 0.925$, $\Theta_{\max} = 0.95$, and $\gamma_{\text{tol}} = 0.90$.

5 Numerical performance for synthetic data

We test the performance of the presented reconstruction algorithm on synthetic as well as experimentally measured data from the Fresnel database. In this section we focus on the synthetic data.

Synthetic data The synthetic data was generated via

$$F_{\text{meas}}^{\delta} = F_{\text{meas}} + \delta\, \frac{\left\|F_{\text{meas}}\right\|_{\text{dis}}}{\|N_{\text{Re}} + \mathrm{i} N_{\text{Im}}\|_{\text{dis}}} \left(N_{\text{Re}} + \mathrm{i} N_{\text{Im}}\right), \tag{73}$$

where $F_{\text{meas}} = \underline{\mathcal{F}}(\underline{q}) \in \mathbb{C}^{N_{\text{s}} \times N_{\text{i}}}$ is the noise free measured data and $N_{\text{Re}}, N_{\text{Im}} \in \mathbb{R}^{N_{\text{s}} \times N_{\text{i}}}$ are two real matrices sampled from standard, normal distribution. Consequently, the considered relative noise level is $\delta = \|F_{\text{meas}}^{\delta} - F_{\text{meas}}\|_{\text{dis}} / \|F_{\text{meas}}\|_{\text{dis}}$.

Relative error To measure the error of the reconstruction the relative error is defined via,

$$\text{err}(m) := \frac{\|q^{(m)} - q_{\text{exa}}\|_2}{\|q_{\text{exa}}\|_2},$$

where q_{exa} is the exact contrast, i. e. the ground truth.

Avoiding the "inverse crime" The inverse crime is a paradigm which describes the effects of the mismatch between the forward operator/physical model assumed for the reconstruction and the "true" model from which the measured data was generated. Of course, in general the reconstruction model is chosen to be more well-behaved than the true model. In practice, this leads to reconstructions which are "too good to be true", see [KS06] or [MS12]. Of course, this is easily avoided if experimentally measured data and ground truth is considered for the performance tests. We do this later on by testing against Fresnel data, see Chapter 6 (p. 29). To avoid the inverse crime for synthetic data, one should generate the synthetic data using a forward solver that has as little as possible to do with the solver employed in the inverse problem, see [CK13, Ch. 5.4]. A simple implementation of this philosophy is to generate the synthetic data using a fine discretization operator and reconstruct the data on a coarse discretization operator, see [MS12, Ch. 2.3.6]. We have used this approach in our experiments for synthetic data. We generated the synthetic data on a computational domain D_{2R} discretized by $N = 1024$ points in each dimension in 2D ($N = 512$ in 3D), and for reconstruction discretized by $N = 256$ (in 2D and 3D).

Setting and parameters The wave number was set to $k = 250$. Consequently, we consider fields with wavelength of about 0.025. Further, we fix 35 identical source/receiver points for incident point sources distributed evenly on a circle with radius 5 centered in the origin. (Near field data is considered for the measurement.) The radius R determining the region of interest D is set to $R = 0.1$ and the computational

domain D_{2R} is discretized by $N = 256$ points in each dimension. Synthetic data is produced with relative noise level $\delta = 0.01$. We set physical bounds assuming that the contrast q satisfies $-1 \leq \mathrm{Re}(q) \leq 3$ and $0 \leq \mathrm{Im}(q) \leq 3$. The exact form of the phantom for the ground truth will be described in Subsection 5.1 for the 2D case and in Subsection 5.2 for the 3D case. If not given explicitly otherwise the regularization parameters of the Tikhonov functional were set to $\alpha = 500$ and $\beta = 10^{-5}$. These parameters were determined manually. A high regularization parameter β influences the operator norm $\|K\|$ (otherwise the discrepancy dominates) and therefore step sizes τ and σ will decrease, which results in a slow iteration. Therefore, we recommend to set firstly $\alpha = 0$ and find a suitable β, and afterwards find a convenient α. Determining the parameters semi-automatically or automatically was outside of the scope of this paper. However, it is the subject of ongoing research. Finally, we remark that all computations were carried out on a workstation with an Intel(R) Core(TM) i7-3770 CPU with 3.40 GHz and 32 GByte RAM.

5.1 Synthetic 2D examples

As the test phantom in 2D we use the scattering object depicted in Fig. 6, that consists of a corner with non-constant contrast q, a ball and a broken corner with $q = 1$. The imaginary part of the phantom vanishes. In what follows we describe the influence of several parameters of the reconstruction algorithm on the reconstruction time and quality as measured by relative discrepancy and relative error.

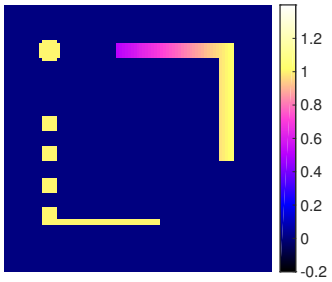

Figure 6: Test phantom for 2D synthetic data (corner with non-constant contrast q, ball and broken corner $q = 1.0$).

Reconstruction of scatterer in imaginary part We observed in case of wave number $k = 250$ that the scatterer appears in the imaginary part (i. e. physical absorption) after the first outer iteration. (This behavior decreases for smaller wavelengths.) Then the scatterer appears successively in the real part. Finally, the imaginary part vanishes as expected. The same behavior is delivered by soft-shrinkage iteration.

Influence of the inner iteration stopping First, in Figure 7 the influence of the stopping criterion for the inner iteration is presented. (The outer iteration was stopped by Morozov's discrepancy principle.) Visually clearly, all three stopping criteria provide similarly satisfactory results. Quantitative description of this similarity is provided by the graphs below. In all three cases the remaining parameters were $\delta = 0.01$, $\alpha = 500$, $\beta = 10^{-5}$, $\tau_{\mathrm{dis}} = 2.5$.

Influence of parameter choices α and β The next step is the study of the influence of the sparsity regularization parameter α and the TV regularization parameter β on the reconstruction time and quality. It is well known that, all other things being equal, the reconstructions will exhibit the typical sparsity or TV artifacts if the related other regularization is switched off by the according parameter is set to zero. In our experience, there is further an interesting dependency between the choice of α and β and related "good" choice of the parameter τ_{dis} in the Morozov's discrepancy principle. In particular, in our experiments a sensible value for τ_{dis} increases/decreases as the values of α and β increase/decrease. This is depicted in Figure 8.

Further we notice, that if $\alpha = 0$ (instead of the default value $\alpha = 500$) the sensible value for τ_{dis} also decreases to 1.5. However, even with this adaptation reconstruction contains obvious "ripples" in the background, see Fig. 8(a). As mentioned above these artifacts are expected in this underregularization case. On the other hand, using $\alpha = 2500$ in Fig. 8(c), the discrepancy parameter had to be increased to $\tau_{\mathrm{dis}} = 6.0$ to stop early enough to get artifact-free reconstruction.

On the other hand, the choice of $\beta = 0$ leads to the reconstruction in Fig. 8(d). In comparison to the reconstruction in Fig. 8(e) one can observe slightly less artifacts in the background, but a hole in the ball. The result of setting $\beta = 5 \cdot 10^{-5}$ is presented in Fig. 8(f). One can observe a hint of "ripples" in the background. Note that it was necessary to set the discrepancy principle parameter to $\tau_{\mathrm{dis}} = 6.0$.

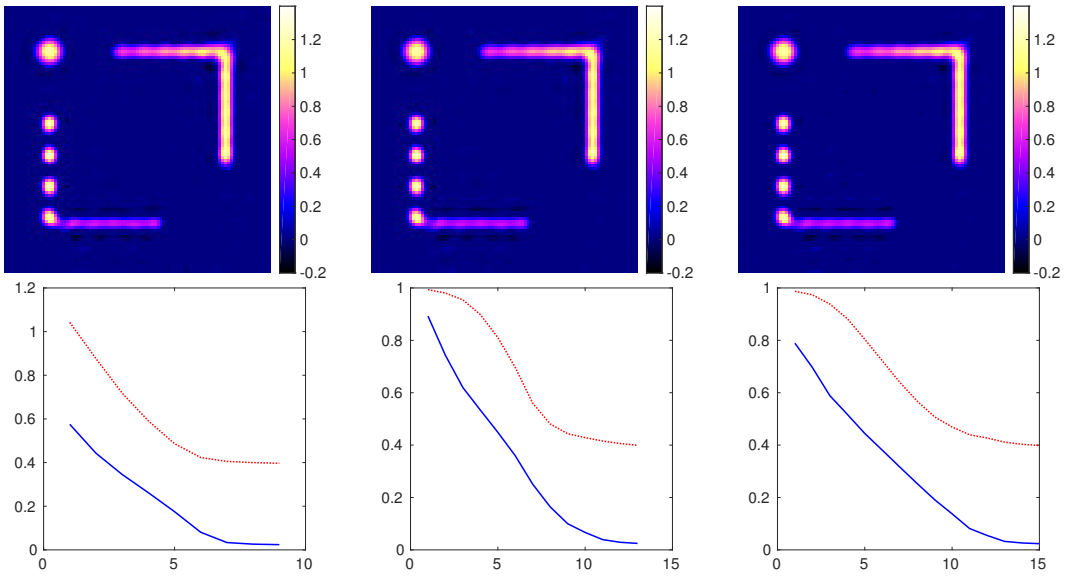

(a) constant. (b) stop. crit. 1. (c) stop. crit. 2.

Figure 7: Effect of the stopping criterion for the inner iterations. Upper row: real part of the reconstructed synthetic contrast. Lower row: relative discrepancy (blue solid) and error (red dotted) as functions of the outer iteration number (x-axis). Run-times, relative discrepancies and relative errors were in (a) 3.3 min, dis. 0.024, err. 0.397, (b) 3.6 min, dis. 0.025, err. 0.399, and (c) 4.1 min, dis. 0.024, err. 0.399.

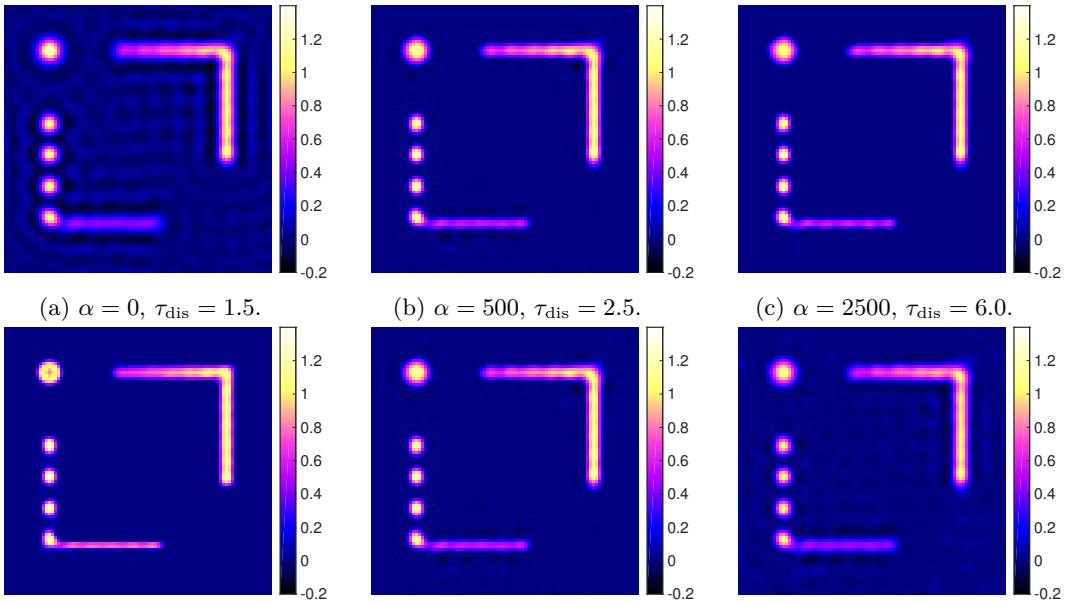

(a) $\alpha = 0$, $\tau_{\text{dis}} = 1.5$. (b) $\alpha = 500$, $\tau_{\text{dis}} = 2.5$. (c) $\alpha = 2500$, $\tau_{\text{dis}} = 6.0$.

(d) $\beta = 0$, $\tau_{\text{dis}} = 1.5$. (e) $\beta = 1 \cdot 10^{-5}$, $\tau_{\text{dis}} = 2.5$. (f) $\beta = 5 \cdot 10^{-5}$, $\tau_{\text{dis}} = 6.0$.

Figure 8: Influence of the sparsity regularization parameter α and the TV regularization parameter β. The upper row deals with changes in α, the lower row with changes in β. If not given explicitly the other parameter is given as $\alpha = 500$, $\beta = 10^{-5}$. In all cases Morozov's discrepancy principle was employed for stopping the outer iteration and stopping criterion 2 for the inner iteration. (Of course the Subfigures (b) and (e) are the same and were duplicated for sake of easier in-row comparison.) Run-times, relative discrepancies and relative errors were in (b) and (e) 3.3 min, dis. 0.024, err. 0.397, in (a) 5.7 min, dis. 0.014, err. 0.446, (c) 2.9 min, dis. 0.056, err. 0.401, (d) 7.9 min, dis. 0.015, err. 0.348, and (f) 2.7 min, dis. 0.057, err. 0.430.

Balanced penalty terms We expect visible effects of the sparsity promoting and TV penalty term, while this penalty terms have the same scale, i. e. they are balanced. The previous choices of regularization parameters as in Fig. 7 and 8 leads into highly unbalanced penalty terms of scale $f_{\text{spa}} = 1$ and $f_{\text{tv}} = 10^{-5}$. Especially for a visible sparsity effect during balanced penalty terms, the primal-dual algorithm needs a high iteration number at least in the last outer step. We demonstrate this in Fig. 9 choosing $\beta = 10^{-5}$ (as before), and comparing $\alpha = 3 \cdot 10^{-3}$ to $\alpha = 0$. For the first 10 outer iterations we employed 50 inner iterations, and for the last outer step $5 \cdot 10^5$ inner iterations, which takes 13 h. For $\alpha = 3 \cdot 10^{-3}$ we see a good reconstruction of the squares, and typical step-artifacts of TV-penalty in the non-constant part of the corner. In this case penalty terms are balanced: $f_{\text{spa}} = 4.2 \cdot 10^{-6}$ and $f_{\text{tv}} = 4.1 \cdot 10^{-6}$. The discrepancy was $f_{\text{dis}} = 3.2 \cdot 10^{-7}$, the relative discrepancy 0.061, and the relative error 0.321. In case of $\alpha = 0$ the relative discrepancy was 0.204, and the relative error 0.519.

To get a rapid algorithm we relinquish the balance of the penalty terms and increase the regularization parameter α to 500 as in the examples before. This enables the utilization of sparsity with a much lower number of inner iterations.

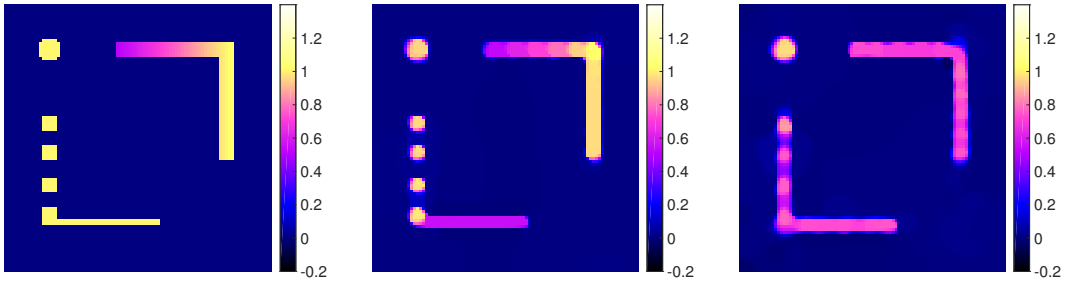

(a) Test phantom as in Fig. 6. (b) $\alpha = 3 \cdot 10^{-3}$. (c) $\alpha = 0$.

Figure 9: Visible effects of the sparsity promoting and TV penalty term, while this penalty terms have the same scale, i. e. they are balanced, are achieved with sparsity regularization parameter $\alpha = 3 \cdot 10^{-3}$ and TV regularization parameter $\beta = 10^{-5}$, see Fig. (b). A comparison to $\alpha = 0$ is given in Fig. (c).

Grid scaling To save CPU time the inversion process for the contrast q can be carried out on a coarser grid than the one used for the wave fields. To that end, the contrast is scaled down for the inversion process, and scaled up for the direct scattering problem. For fast downscaling we employed the MATLAB function `imresize` with interpolation method `nearest` in 2D. In case of 3D we applied `imresize` on the slices of the grid. To analyze the effects of this approach we considered with fixed 9 outer iterations (and fixed number of inner iterations) to compare it to the example from Fig. 7(a). The related reconstruction with halved number of discretization points in each dimension for the inversion process is depicted in Fig. 10. Altogether, a slight speed up can be reported (about 15 %), but the reconstruction quality significantly decreased.

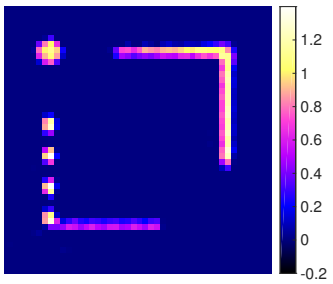

Figure 10: Reconstruction with grid scaling (halved number of discretization points in each dimension for inversion).

5.2 Synthetic 3D examples

In the last part of this section we consider synthetic 3D data. To this end, we consider two phantoms. First a "tripod" phantom, see Fig. 11(a), with contrast $q = 1.0$ in the first horizontal arc, $q = 0.8$ in the second one, and $q = 0.6$ in the (entire) vertical one. The second "cross" phantom, see Fig. 11(i), has the following properties: the first horizontal bar has a contrast $q = 0.8$, the second one $q = 0.6$, and the vertical one $q = 1.0$. To our best knowledge, the reconstruction of the second phantom is especially challenging.

In both cases the same reconstruction parameters were employed. The radius determining the computational domain D is set to $R = 1$. The computational domain is discretized by $N = 256$ points in every dimension. Further, near field data is used, with 50 transmitters and receivers distributed on a circle with

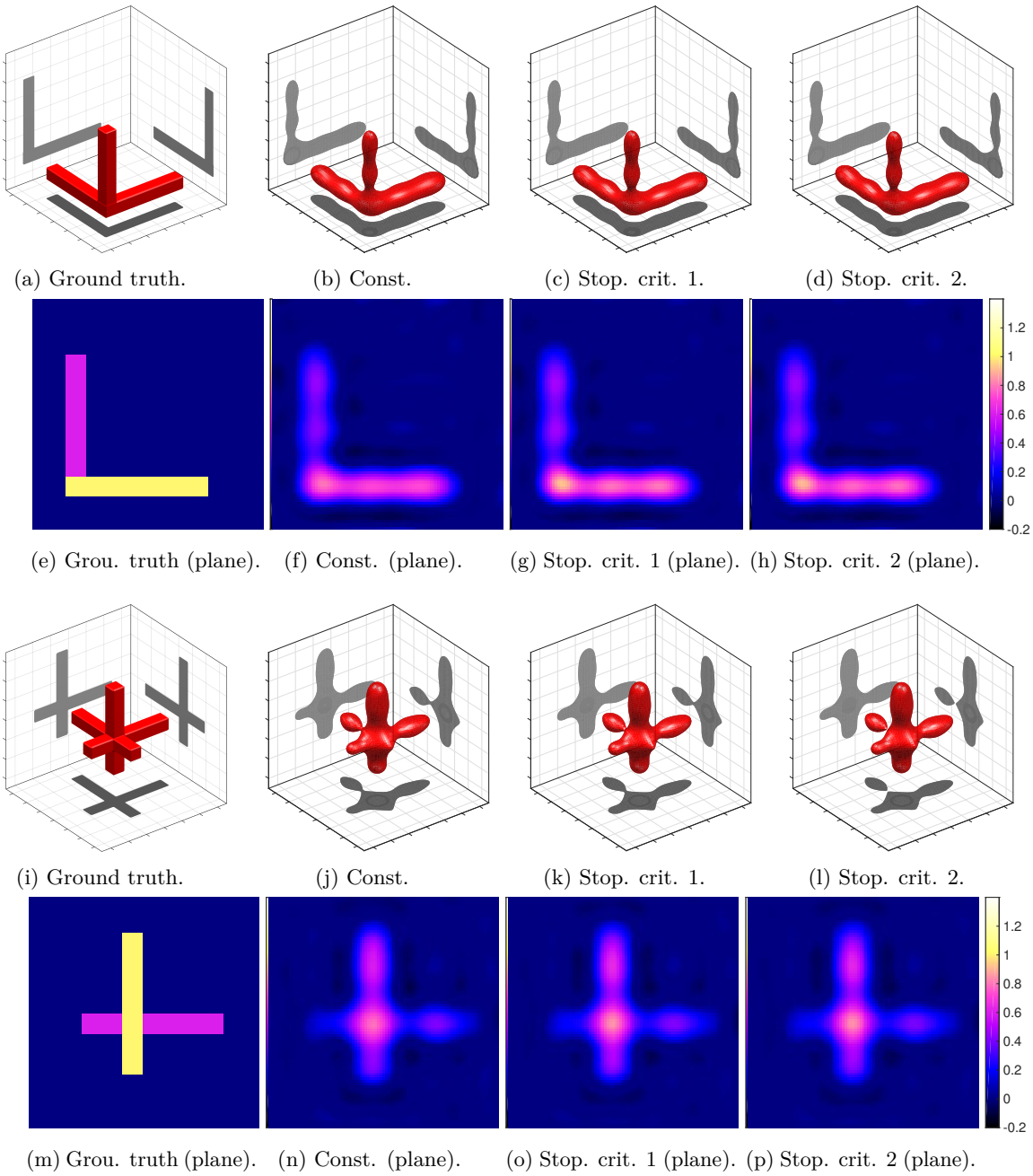

(a) Ground truth. (b) Const. (c) Stop. crit. 1. (d) Stop. crit. 2.

(e) Grou. truth (plane). (f) Const. (plane). (g) Stop. crit. 1 (plane). (h) Stop. crit. 2 (plane).

(i) Ground truth. (j) Const. (k) Stop. crit. 1. (l) Stop. crit. 2.

(m) Grou. truth (plane). (n) Const. (plane). (o) Stop. crit. 1 (plane). (p) Stop. crit. 2 (plane).

Figure 11: Influence of the stopping criterion for the inner iteration. In all cases the real part of ground truth/reconstruction for the tripod phantom (top row) and cross phantom (bottom row) is depicted. Further, in all cases, the employed parameters were $\delta = 0.01$, $\alpha = 500$ and $\beta = 10^{-5}$, $\tau_{\text{dis}} = 1.25$. For visualization we computed isosurface data with isosurface value 0.3, see (a)–(d) and (i)–(l). The contrast on a sectional plane through the scatterer is presented in (e)–(h) (plane through 1^{st} horizontal and vertical arm) and (m)–(p) (plane through 2^{nd} horizontal and vertical arm). Run-times, relative discrepancies and relative errors were in (b)/(f) 4.8 h, dis. 0.012, err. 0.635, (c)/(g) 4.4 h, dis. 0.011, err. 0.606, (d)/(h) 6.6 h. dis. 0.012, err. 0.619, (j)/(n) 5.3 h, dis. 0.012, err. 0.656, (k)/(o) 4.4 h, dis. 0.011, err. 0.636, (l)/(p) 6.5 h, dis. 0.012, err. 0.649.

radius 5 around the target. The wave number is set to $k = 10$, such that the wavelength roughly equals 0.63. As in the 2D case we use the relative noise level $\delta = 0.01$, physical bounds $-1 \leq \mathrm{Re}(q) \leq 3$ and $0 \leq \mathrm{Im}(q) \leq 3$. The regularization parameters $\alpha = 500$ and $\beta = 10^{-5}$ turned out to be suitable for the reconstruction process. Further, we set $\tau_{\mathrm{dis}} = 1.25$ to stop the outer iteration by discrepancy principle. For the inner stopping criteria the same default settings as in the 2D case were employed.

The results for both phantoms are depicted in Fig. 11. In particular, we focus on the dependency of the quality and efficiency of the reconstruction scheme with respect to the stopping criterion in the inner iteration. Run-times, relative discrepancies and relative errors are given in the caption. The only difference was noticeable for the run-times.

6 Numerical performance on measured data

In this final section, we test the presented reconstruction algorithm with experimentally measured two-dimensional data published by the Institute Fresnel in a special issue of the journal *Inverse Problems*, see [BS01]. We sum up the main parameters of the Fresnel data set. The part of the data set employed for our reconstruction scheme consists of scattering of electromagnetic waves from long cylindrical objects in TM polarization. The transmitters and receivers are distributed on a circle around the scatterer. In particular, the data set contains the measurements of real and imaginary part of the total electric field $u^{\mathrm{t}}|_{\Gamma_{\mathrm{s}}}$ and the incident field $u^{\mathrm{i}}|_{\Gamma_{\mathrm{s}}}$ on a circle Γ_{s} with radius of $760 \pm 3\,\mathrm{mm}$ around the scattering object. The distance between the transmitter and the centre of the experimental set-up is $720 \pm 3\,\mathrm{mm}$. Of course, for measurements of the incident field, no scattering object is present and the incident field merely illuminates the experimental set-up.

The measurements were devised in an anechoic chamber. In the realization of the Institute Fresnel, the transmitter is fixed and emits incident fields while the scatterer is rotated and the receiver (a double ridged horn antenna) is moved on a circular rail around the scatterer. The experimental set-up prevents the receiver from getting close to the transmitter (the aperture is 240°). Thus, in dependence of the employed transmitter, several receiver measurements are missing. Further details of the experimental set-up, in particular details on the geometry, can be found in [BS01]. We give an illustration of the experimental set-up in Fig. 12. For this set-up, the multi-static scattering data is hence contained in an array $F^{\delta}_{\mathrm{meas}} \in \mathbb{C}^{N_{\mathrm{s}} \times N_{\mathrm{i}}}$. It includes $N_{\mathrm{i}} = 36$ field measurements corresponding to 36 transmitter positions in its columns. Each column vector includes $N_{\mathrm{s}} = 49$ measurements at receiver positions depending on the transmitter position. Note, however, that the transmitter/receiver set-up is merely rotated from one measurement to the next one, such that the angles in between any transmitter/receiver are the same for each measurement.

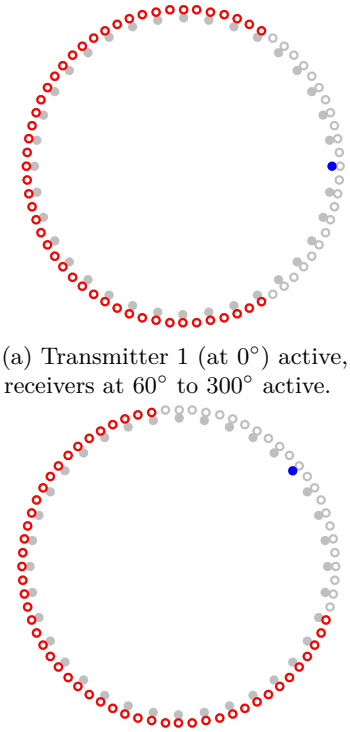

(a) Transmitter 1 (at 0°) active, receivers at 60° to 300° active.

(b) Transmitter 5 (at 40°) active, receivers at 100° to 340° active.

Figure 12: Experimental set-up for Fresnel data: transmitters in 10° steps (inner circle) and receivers in 5° steps (outer circle). Active receivers (red) are shown for two positions of active transmitters (blue).

For simplicity, we denote in the following each individual measurement (which is a complex vector of length $N_{\mathrm{s}} = 49$) of the total and incident field by $u^{\mathrm{t}}|_{\Gamma_{\mathrm{s}}}$ and $u^{\mathrm{i}}|_{\Gamma_{\mathrm{s}}} \in \mathbb{C}^{N_{\mathrm{s}} \times 1}$. In particular we omit the variable receiver positions in the notation, as the appropriate setting is clear from the context.

6.1 Matching the incident fields

The forward operator discussed in Sections 3.5 and 3.6 was designed for point sources. However, the Fresnel data set was generated by real-word antennae. This necessitates to deduce the incident field on the region of interest D from the measurements $u^{\mathrm{i}}|_{\Gamma_{\mathrm{s}}}$ of that field at the receivers. In consequence, to apply

our reconstruction scheme to the Fresnel data set we must change/match the functions employed in the single-layer potential operator, cf. Section 3.5.

A multi-pole model for incident point sources As the measurement set-up is rotation invariant, it is sufficient to detail this matching procedure merely for a single unknown incident field generated by a point source on Γ_i, which yields measurements $u^\mathrm{i}|_{\Gamma_\mathrm{s}}$ at N_s receivers with positions $B_j \in \mathbb{R}^2$, $j = 1, \dots, N_\mathrm{s}$. By shifting the coordinate system, we can moreover assume that the source position is the origin.

Let us then denote polar coordinates corresponding to (x, y) as (φ, r), represent B_j as (r_j, φ_j), and consider the Hankel functions $H_\nu^{(1)}$ of the first kind and order $\nu \in \mathbb{Z}$. It is then well-known that the products

$$\mathcal{H}_\nu(\varphi, r) = \frac{\mathrm{i}}{4} H_\nu^{(1)}(kr) \exp(\mathrm{i}\nu\varphi), \quad r > 0,\ \varphi \in [0, 2\pi),$$

as well as any linear combination of these products, are solutions of the Helmholtz equation (3) in $\mathbb{R}^2 \setminus \{0\}$ that satisfy Sommerfeld's radiation condition, see [CK13]. We use these solutions to match the measured incident fields at the receiver positions.

To this end, we choose $\xi \in \mathbb{N}$ to restrict ν to the $2\xi + 1$ values $\nu = -\xi, \dots, +\xi$, represent a synthetic incident field as $(\varphi, r) \mapsto \sum_{\nu=-\xi}^{+\xi} c_\nu \mathcal{H}_\nu(\varphi, r)$, and seek coefficients $c_\nu \in \mathbb{C}$ such that this synthetic incident field matches the measurements $u^\mathrm{i}|_{B_j}$,

$$u^\mathrm{i}|_{B_j} \stackrel{!}{=} \sum_{\nu=-\xi}^{+\xi} c_\nu \mathcal{H}_\nu(\varphi_j, r_j), \quad j = 1, \dots, N_\mathrm{s}. \tag{74}$$

Defining the matrix $\mathcal{V} \in \mathbb{C}^{N_\mathrm{s} \times (2\xi+1)}$ by $\mathcal{V}_{j,\nu} = \mathcal{H}_\nu(\varphi_j, r_j)$ for $j = 1, \dots, N_\mathrm{s}$, $\nu = -\xi, \dots, \xi$ we hence seek a coefficient vector $c = (c_{-\xi}, \dots, c_{+\xi})^\top \in \mathbb{C}^{(2\xi+1)\times 1}$ such that

$$\mathcal{V}c \approx u^\mathrm{i}|_{\Gamma_\mathrm{s}}. \tag{75}$$

Given c, the incident field on the region of interest D is given via $u^\mathrm{i}|_D = \sum_{\nu=-\xi}^{+\xi} c_\nu \mathcal{H}_\nu(\varphi, r)|_D$.

Solving for suitable coefficients Obviously, it is very important to recover the coefficients c exactly. Otherwise the forward operator is not generating the measured data. Consequently, the reconstruction algorithm will inevitably fail. Of course, the problem can be underdetermined as well as overdetermined depending on the size of ξ. In general, the problem will be ill-conditioned. Therefore, to get suitable coefficients c we tested three recovery/regularization methods tackling the approximation problem (75).

The first one, denoted as (M1), computes the best-approximation to (75) in case the system is overdetermined, and the least-squares solution if it is underdetermined. The second method (M2) computes $c = (\gamma I + \mathcal{V}^*\mathcal{V})^{-1}(\mathcal{V}^* u^\mathrm{i}|_{\Gamma_\mathrm{s}})$ via linear Tikhonov regularization with a small $\gamma > 0$. The third method (M3) relies on the Landweber iteration stopped after 10^5 respectively 10^8 iterations to solve (75). See e. g. [MS12] for more background on these regularization methods.

Freq. in GHz	Method, iterations	Rel. err. of $\mathcal{V}c = u^\mathrm{i}\|_{\Gamma_\mathrm{s}}$ in % mean	Rel. err. of data in % real part	imag. part
3	(M1)	1.3	14.9	15.3
3	(M2)	1.8	15.0	15.7
3	(M3), 10^5	1.6	14.9	15.7
3	(M3), 10^8	1.5	14.9	15.5
5	(M1)	3.4	20.1	22.4
5	(M2)	21.2	20.5	26.9
5	(M3), 10^5	15.2	19.1	23.1
5	(M3), 10^8	10.4	18.8	21.2

Table 1: Comparison of methods computing coefficients c using Fresnel data of a single dielectric `dielTM_dec8f.exp` and $\xi = 10$. We give the relative error of the measured incident field $u^\mathrm{i}|_{\Gamma_\mathrm{s}}$ as well as the relative error of data taking into account the manually corrected position of the target, see Section 6.2.

For the Fresnel data set (3 GHz respectively 5 GHz data) and $\xi = 10$ the relative errors of the matched fields are listed in Table 1. Notice that also error of the measured data is provided. This is possible since the corresponding "ground truth" about the scattering objects is known from [BS01]. Therefore, it is possible

to simulate the related data matrix. However, it must be noted that we take into account the manually corrected position of the target, see Section 6.2. We display only the mean relative error for all incident fields because the minimal and maximal errors do not differ significantly. Obviously, the first method (M1) outperforms the other two methods. As the indicated errors for (M1) do not decrease by further increasing the value of ξ, we hence match all incident fields using (M1) with $\xi = 10$.

6.2 Reconstruction of the target using Fresnel data

We consider the cases of single dielectric respectively two dielectrics as targets. In experiment, the real part of the contrast of the target is $q = 2 \pm 0.3$. Since the targets are dielectric the imaginary part vanishes, see [BS01, Ch. 4.2]. Further, according to [BS01, Ch. 4.2] the radius of the filled dielectric cylinders is 15 mm, the position of the centre of the single dielectric is left to the origin with a distance of 30 mm from the origin, and the two dielectrics sit left and right to the origin (on the x_1-axis) with a distance of 45 mm from the origin.

However, even rough reconstructions show that the above mentioned positions have to be slightly changed to describe the recorded data. First, it is observed that the targets have to be rotated 270° in mathematical positive direction. Further, the single dielectric is shifted by 1 mm to the right and by 3 mm downwards, see Fig. 13(a). Also, for the two dielectrics case a shift by 8 mm to the left and 1 mm upwards as well as a rotation of 8° in mathematical positive direction is necessary to get a suitable position, see Fig. 13(b). In what follows, that the manually corrected positions are employed for the computation of the relative data errors in Tab. 2.

For the reconstruction, the grid size is $N = 256$ in every dimension. The regularization parameters are empirically derived to be $\alpha = 500$ and $\beta = 10^{-5}$ and the physical bounds are $-1 \leq \mathrm{Re}(q) \leq 3$ and $0 \leq \mathrm{Im}(q) \leq 1$. Notice that to stop the outer iteration by Morozov's discrepancy principle, see (72), one needs to know an estimate of the noise level δ. We estimate the noise level by comparing the measured data to the data produced by manually corrected positions (see last paragraph).

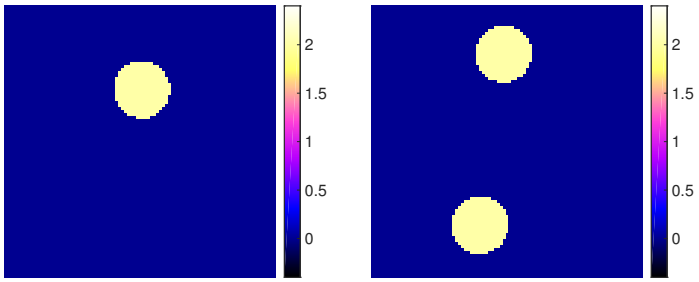

(a) One dielectric. (b) Two dielectrics.

Figure 13: The real part for the two "ground truth" contrast considered here as part of the Fresnel data set. The positions were manually corrected.

Frequency	Rel. err. of $\mathcal{V}c = u^{\mathrm{i}}\|_{\Gamma_{\mathrm{s}}}$ in % mean	Rel. err. of data y in % real part	imag. part
single dielectric (`dielTM_dec8f.exp`)			
1 GHz	0.9	29.8	39.7
2 GHz	0.6	18.0	14.9
3 GHz	1.3	14.9	15.3
4 GHz	0.8	25.2	19.7
5 GHz	3.4	20.1	22.4
6 GHz	4.2	39.7	32.7
7 GHz	16.4	22.2	28.1
8 GHz	18.1	44.3	39.1
two dielectrics (`twodielTM_8f.exp`)			
1 GHz	1.0	11.5	64.5
2 GHz	0.6	46.7	8.1
3 GHz	1.3	13.4	21.6
4 GHz	0.8	47.9	15.6
5 GHz	3.3	20.3	27.4
6 GHz	4.0	59.5	36.8
7 GHz	16.1	25.2	42.9
8 GHz	17.8	72.2	41.1

Table 2: Relative error of the measured incident field $u^{\mathrm{i}}|_{\Gamma_{\mathrm{s}}}$ and the relative error of data for the manually corrected positions of the targets, see Section 6.2 for different frequencies. In every case, the related c for the matched incident field were computed by best-approximation method (M1) and $\xi = 10$.

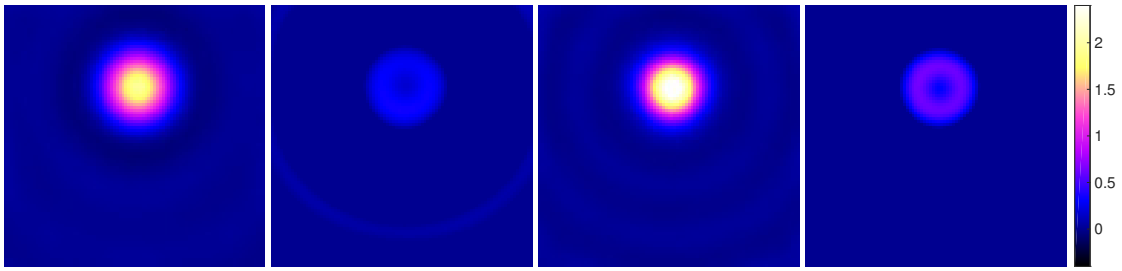

(a) 3 GHz, real part. (b) 3 GHz, imag. part. (c) 5 GHz, real part. (d) 5 GHz, imag. part.

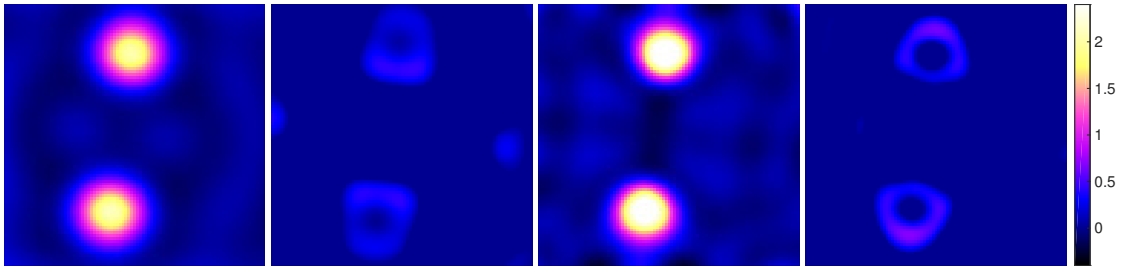

(e) 3 GHz, real part. (f) 3 GHz, imag. part. (g) 5 GHz, real part. (h) 5 GHz, imag. part.

Figure 14: Reconstructions of the experimentally measured data set of Institute Fresnel for the one dielectric case (top row) and two dielectric case (bottom row) for two frequencies. In both cases the parameters described in the text were employed. The related "ground truth" are given in Fig. 13.

Target	Freq.	Noise level δ	Inner stop. crit.	N_{out}	Run-time	Rel. dis.	Rel. err.
single dielectric	3 GHz	15 %	1	7	1.3 min	0.239	0.547
single dielectric	5 GHz	20 %	1	7	1.4 min	0.267	0.564
two dielectrics	3 GHz	15 %	1	7	1.4 min	0.234	0.541
two dielectrics	5 GHz	25 %	1	7	1.6 min	0.245	0.513

Table 3: Quantitative performance of the reconstruction scheme for the Fresnel data set in two dimensions published by the Institute Fresnel with our choice of noise levels. The noise level was estimated by the method described in text.

Approximation of the relative data error with single and two dielectrics As can be seen in Table 2 and as expected the incident field matching is especially successful in the low frequency range. In particular, for frequencies 1–4 GHz the relative error is maximally 1.3 %, for 5 and 6 GHz under 5 %, while at the higher frequencies 7 and 8 GHz it exceeds 15 %. In contrast, no clear trend is present in the relative data error. In this light, we have selected in both single and two dielectrics cases 3 and 5 GHz as the most promising cases for the test of our reconstruction scheme. Based on the relative data error the values in Table 3 are chosen as noise levels to stop the outer iteration by the discrepancy principle with $\tau_{\text{dis}} = 1.6$, see (72). In Figure 14 the reconstructions for the above mentioned targets and frequencies are presented for the case of stopping the inner iteration by stopping criterion 1. The related quantitative evaluation can be found in Table 3. The reconstructions for the constant stopping criterion with $N_{\text{in}} = 10$ and stopping criterion 2 were very similar, qualitatively (visually) as well as quantitatively (run-times, relative discrepancies, relative errors). We therefore omit them here.

Measured data in three dimensions The Institute Fresnel published electromagnetic scattering data of three-dimensional targets for transverse magnetic (TM) and transverse electric (TE) polarization. Actually,

our model can only deal with TM polarized data in the two-dimensional case, see Sec. 2 (p. 3). In three dimensions we would have to take into account TM and TE polarized data, see [LAv09]. This would in any case require a numerical solver for the three-dimensional Maxwell's equations.

7 Summary

We derived an minimization-based iterative inversion algorithm for inverse medium scattering problems. The direct scattering problem is treated by volume integral equations that allow to rapidly set up Fréchet derivatives. To stop the outer and inner iteration of the scheme we rely on the discrepancy principle and adapted tolerance principles. Numerical experiments for scattering in two and three dimensions showing the quality of reconstruction were provided for synthetic data. Furthermore, the performance of the reconstruction method was tested for experimentally measured data from Institute Fresnel.

Acknowledgements The research of all authors was supported by the German Research Foundation (DFG) under grants Ka 3954/1-1 and Le 2499/2-1.

References

[BH15] Kristian Bredies and Martin Holler. A TGV-based framework for variational image decompression, zooming, and reconstruction. Part II: Numerics. *SIAM Journal on Imaging Sciences*, 8(4):2851–2886, 2015.

[BL06] Jonathan Borwein and Adrian Lewis. *Convex Analysis and Nonlinear Optimization*. CMS Books in Mathematics. Springer, New York, second edition, 2006.

[BL11] Kristian Bredies and Dirk Lorenz. *Mathematische Bildverarbeitung: Einführung in Grundlagen und moderne Theorie*. Vieweg+Teubner, 2011.

[BS01] Kamal Belkebir and Marc Saillard. Special section on testing inversion algorithms against experimental data. *Inverse Problems*, 17(6):1565–1571, 2001.

[Buk08] Alexander L. Bukhgeim. Recovering a potential from Cauchy data in the two-dimensional case. *Journal of Inverse and Ill-posed Problems*, 16(1), 2008.

[CK13] David Colton and Rainer Kress. *Inverse Acoustic and Electromagnetic Scattering Theory*. Springer, New York, 2013.

[CP11] Antonin Chambolle and Thomas Pock. A first-order primal-dual algorithm for convex problems with applications to imaging. *Journal of Mathematical Imaging and Vision*, 40(1):120–145, 2011.

[DDD04] Ingrid Daubechies, Michel Defrise, and Christine De Mol. An iterative thresholding algorithm for linear inverse problems with a sparsity constraint. *Communications on Pure and Applied Mathematics*, 57(11):1413–1457, 2004.

[dLS+16] Maarten de Hoop, Matti Lassas, Matteo Santacesaria, Samuli Siltanen, and Janne P. Tamminen. Positive-energy D-bar method for acoustic tomography: a computational study. *Inverse Problems*, 32(2):025003, 2016.

[EHN96] Heinz W. Engl, Martin Hanke, and Andreas Neubauer. *Regularization of inverse problems*. Kluwer Academic Publishers, Dordrecht, Netherlands, 1996.

[FJ05] Matteo Frigo and Steven G. Johnson. The design and implementation of FFTW3. *Proceedings of the IEEE*, 93(2):216–231, 2005. Special issue on "Program Generation, Optimization, and Platform Adaptation".

[Häh96] Peter Hähner. A periodic Faddeev-type solution operator. *Journal of Differential Equations*, 128:300–308, 1996.

[HH14] Thorsten Hohage and Carolin Homann. A generalization of the Chambolle-Pock algorithm to Banach spaces with applications to inverse problems. arXiv:1412.0126, 2014.

[Hoh01] Thorsten Hohage. On the numerical solution of a three-dimensional inverse medium scattering problem. *Inverse Problems*, 17(6):1743, 2001.

[KG08] Andreas Kirsch and Natalia Grinberg. *The Factorization Method for Inverse Problems*. Oxford Lecture Series in Mathematics and its Applications 36. Oxford University Press, 2008.

[KS03] Steven Kusiak and John Sylvester. The scattering support. *Communications on Pure and Applied Mathematics*, 56(11):1525–1548, 2003.

[KS06] Jari Kaipio and Erkki Somersalo. *Statistical and Computational Inverse Problems*. Applied Mathematical Sciences. Springer, New York, 2006.

[LAv09] Maokun Li, Aria Abubakar, and Peter M. van den Berg. Application of the multiplicative regularized contrast source inversion method on 3D experimental Fresnel data. *Inverse Problems*, 25(2):024006, 2009.

[LKK13] Armin Lechleiter, Kamil S. Kazimierski, and Mirza Karamehmedović. Tikhonov regularization in L^p applied to inverse medium scattering. *Inverse Problems*, 29(7):075003, 2013.

[LMM12] Dirk A. Lorenz, Peter Maaß, and Pham Q. Muoi. Gradient descent methods based on quadratic approximations of Tikhonov functionals with sparsity constraints: theory and numerical comparison of stepsize rules. *Electronic Transactions on Numerical Analysis*, 39:437–463, 2012.

[LN11] Armin Lechleiter and Dinh-Liem Nguyen. Spectral volumetric integral equation methods for acoustic medium scattering in a 3D waveguide. *IMA Journal of Numerical Analysis*, 32(3):813–844, 2011.

[Mat] MathWorks. MATLAB documentation. http://de.mathworks.com/help/matlab/. Accessed: 2015-11.

[MS12] Jennifer L. Mueller and Samuli Siltanen. *Linear and Nonlinear Inverse Problems with Practical Applications*. Computational Science & Engineering. SIAM, Philadelphia, 2012.

[PCBC09] Thomas Pock, Daniel Cremers, Horst Bischof, and Antonin Chambolle. An algorithm for minimizing the piecewise smooth Mumford-Shah functional. In *IEEE International Conference on Computer Vision (ICCV)*, pages 1133–1140, 2009.

[Rie03] Andreas Rieder. *Keine Probleme mit Inversen Problemen*. Vieweg, Wiesbaden, 2003.

[Roc67] R. Tyrrell Rockafellar. Duality and stability in extremum problems involving convex functions. *Pacific Journal of Mathematics*, 21(1):167–187, 1967.

[RW98] R. Tyrrell Rockafellar and Roger J.-B. Wets. *Variational Analysis*. Grundlehren der mathematischen Wissenschaften. Springer, Berlin, Heidelberg, 1998.

[SKHK12] Thomas Schuster, Barbara Kaltenbacher, Bernd Hofmann, and Kamil S. Kazimierski. *Regularization Methods in Banach Spaces*, volume 10 of *Radon Series on Computational and Applied Mathematics*. De Gruyter, Berlin, 2012.

[Vai00] Gennadi Vainikko. Fast solvers of the Lippmann-Schwinger equation. In Robert P. Gilbert, Joji Kajiwara, and Yongzhi S. Xu, editors, *Direct and Inverse Problems of Mathematical Physics*, volume 5 of *International Society for Analysis, Applications and Computation*, pages 423–440. Springer, New York, 2000.